

EUV Lithography System with Diffraction Optics

Kenneth C. Johnson, November 4, 2021

ABSTRACT

A maskless, extreme ultraviolet (EUV) lithography scanner uses an array of microlenses, such as binary-optic, zone-plate lenses, to focus EUV radiation onto an array of focus spots (e.g. about 2 million spots), which are imaged through projection optics (e.g., two EUV mirrors) onto a writing surface (e.g., at 6X reduction, numerical aperture 0.55). The surface is scanned while the spots are modulated to form a high-resolution, digitally synthesized exposure image. The projection system includes a diffractive mirror, which operates in combination with the microlenses to achieve point imaging performance substantially free of geometric and chromatic aberration. Similarly, a holographic EUV lithography stepper can use a diffractive photomask in conjunction with a diffractive projection mirror to achieve substantially aberration-free, full-field imaging performance for high-throughput, mask-projection lithography. Maskless and holographic EUV lithography can both be implemented at the industry-standard 13.5-nm wavelength, and could potentially be adapted for operation at a 6.7-nm wavelength.

BACKGROUND

EUV lithography has been under development for two decades, primarily by the Netherlands-based company ASML, which is currently the sole global supplier of commercial EUV lithography systems. A mask-projection lithography scanner of the type manufactured by ASML directs EUV illumination at a 13.5-nm wavelength onto a reflective photomask, which is scanned across the stationary illumination field and is imaged at 4X reduction onto a writing surface, a 300-mm semiconductor wafer. The wafer is also synchronously scanned in the opposite direction to maintain a fixed positional relation between the image and the wafer. The mask and wafer are scanned at a relative speed of about 2 meters per second while their alignment is dynamically controlled to nanometer-scale accuracy. (This level of synchronization accuracy requires compensation for the finite speed of light.) The imaging is performed by a six-mirror projection system. Strick tolerances on optical aberrations require atomic-scale surface shape

accuracies over mirrors up to 1-meter diameter. (This is comparable to holding a sub-millimeter shape tolerance over an aperture as large as the continental United States.)

ASML's newest EUV mask-projection scanner, the EXE-5000, which is expected to start shipping in 2023, will have print resolution down to 8-nm half-pitch and print throughput up to 185 wafers per hour. This performance level will come at a cost of about \$250 million per system, plus mask costs of order \$500,000 each.

Much of the complexity and expense of lithography scanners ("step-and-scan" systems) stems from the need to cover a full wafer die, measuring 26 by 33 mm, in a single scan pass. High-resolution, wide-field imaging is achieved by confining the illumination to a narrow, arc-shaped "ring field" on the mask, across which the mask scans to achieve full-area coverage. Older "steppers" ("step-and-repeat" systems) from the early days of lithography, which image the full mask aperture in a single static exposure step (without scanning), are more limited in how large an image field can be covered with acceptable optical resolution. However, the EXE-5000 relinquishes the full-field scan advantage: It only covers a 26-by-16.5-mm image field in one scan pass and uses field stitching to cover a full 26-by-33-mm die. (Two separate masks are required to pattern the full die field.)

The cost-effectiveness of EUV scanners is limited by power and low optical efficiency, which can, in some cases, necessitate a significant throughput reduction to achieve adequate exposure dose. Also, print quality can be limited by optical shadowing ("3-D effects") in EUV masks resulting from oblique illumination on the mask, which is required to separate the incident and reflected light

The primary alternative to EUV for high-resolution patterning is e-beam lithography, which is less expensive and does not use photomasks, but which has throughput about four orders of magnitude slower than EUV lithography. A primary application of e-beam lithography is EUV mask manufacture ("mask writing"). IMS Nanofabrication (an Austrian subsidiary of Intel Corp.) manufactures a multibeam mask writer, which uses approximately 250,000 parallel e-beam channels to achieve throughput of about 10 hours per mask.

U.S. Patent 9,097,983 (hereafter '983) and more recent publications (Ref's. 1, 2) disclose a maskless EUV lithography system, which could achieve throughput 2 to 4 times faster than e-beam for mask-writing. This is well below the throughput of mask-projection lithography, but maskless

EUV could provide an exposure dose level much higher than either e-beam or mask-projection EUV.

The maskless system uses an EUV microlens array with about 2 million microlens channels, in lieu of a photomask, to condense EUV illumination onto discrete focal points, which are imaged through projection optics onto a writing surface. The surface is raster-scanned across the focus-point array as the points are individually modulated to construct a digitally synthesized exposure image. The surface scan speed is relatively low, e.g. a few millimeters per second. (Only the writing surface is scanned; the microlens array remains stationary.)

The microlenses can be configured to offset and neutralize geometric optical aberrations in the projection system, resulting in relaxed design requirements for the EUV mirrors. Consequently, the maskless system requires only two projection mirrors compared to the six mirrors of commercial EUV mask-projection systems. The benefits of a simplified projection system include lower cost, higher optical efficiency, and comparatively relaxed mirror fabrication tolerances.

The relatively high optical efficiency and high exposure dose of maskless EUV could make it possible to adapt the system for operation at a reduced wavelength of 6.7 nm, which would improve optical resolution by 2X relative to conventional 13.5-nm EUV lithography. (Wavelength reduction might not be feasible for conventional EUV mask-projection lithography due to the very low refractive index contrast of available optical materials for 6.7 nm, which would result in severe mask 3-D effects and a drastic reduction in the EUV mirrors' reflection bandwidth; Ref's. 3 and 4.)

EUV lithography systems use laser-produced plasma (LPP) EUV light sources, which have a broad spectral band. The system transmission bandwidth is 2% of the 13.5-nm operating wavelength for mask-projection EUV lithography, and somewhat higher – 3% – for maskless (according to Ref. 2) due to the higher optical efficiency. This creates a problem for maskless lithography because the EUV microlenses are diffractive devices (similar to diffraction gratings), which exhibit significant chromatic aberration over the 3% transmission band. This limitation could be overcome with a two-stage achromatic lens design (a “Schupmann doublet”; see Fig. 10 in the '983 patent and page 9 in Ref. 1). This would require aligned microlenses formed on opposite sides of a microchannel plate, with micromechanical shutters and data paths sandwiched between the two lens planes. Also, the second lens element in each doublet (the downstream element in the optical path) would need to be accurately blazed to concentrate transmitted light in a

first diffraction order with very little optical scatter into other orders. Such lenses are relatively difficult to manufacture relative to binary-optic zone-plate lenses that are more commonly used for EUV applications (Ref. 5).

Another nonstandard lithography method that also makes use of diffractive optics for pattern generation is holographic lithography. U.S. Patent 7,499,149 discloses “a lithographic apparatus and a mask, especially for use with EUV radiation, that is less susceptible to imaging defects caused by dust or damage.” The mask is a “holographic patterning device” positioned “in a plane displaced from the best object plane of the projection system” in the lithographic apparatus. The impact of “dust particles or localized damage” on the mask is minimal because the mask is not imaged sharply on the writing surface.

Deuter (Ref. 6) discloses “Holographic Masks for Proximity Lithography Using EUV Radiation”. In this system the mask is positioned in close proximity to the writing surface without intervening projection optics. Cheng and Isoyan (Ref's. 7, 8) similarly disclose holographic EUV masks that operate without projection optics, and Borisov (Ref. 9) discloses a holographic mask with a visible-light operating wavelength.

SUMMARY

The following disclosure outlines a new EUV maskless lithography design that uses an array of microlenses to focus EUV illumination onto a corresponding array of focus spots, which are imaged through projection optics (one or more EUV mirrors) onto a writing surface. The surface is scanned and the spots are modulated, in the manner taught by '983 and Ref's. 1 and 2, to form a digitally synthesized exposure image. However, the lenses need not be achromatic in the new design; their chromatic effects can be significantly offset and neutralized by constructing at least one mirror element in the projection optics as a diffractive element.

The lenses can be simple binary-optic zone-plate lenses, similar to lenses that are commonly used for EUV applications. The lenses are formed on one side of a microchannel plate with hollow light-transmission channels, and any optical scatter in extraneous diffraction orders is blocked by the plate or by a spatial-filter aperture array at the lens focal plane on the opposite side of the plate. Micromechanical shutters can also be disposed proximate the lens foci to modulate the individual lens-transmitted beams.

The lenses can alternatively be blazed to concentrate most of the light transmitted through each lens into a single diffraction order, which is directed through the lens focus. This could

approximately double the optical efficiency relative to binary-optic lenses. Furthermore, if the lenses do not generate any significant optical scatter within the projection system's angular acceptance range, then it would also be possible to eliminate the spatial-filter apertures and the microchannel plate, leaving the microlenses on an edge-supported, thin-film substrate (a kind of "patterned pellicle"). In this configuration the pattern need not have the form of a microlens array; any kind of diffractive structure can be used to form an arbitrary full-field image, not just a point-array image. The microlens array is thus transformed into an EUV transmission photomask for holographic mask-projection (not maskless) lithography. (The design can alternatively be configured to use a reflection mask.)

In this operational mode the illumination need not be modulated and the image pattern is not scanned; it is statically projected onto the writing surface to expose a full image field. Larger fields of unlimited size can be exposed via field stepping and stitching. The mask is "holographic" because it is not imaged directly onto the writing surface; it operates via diffraction to form an optical pattern on the projection system's object plane, which is imaged onto the writing surface. (The mask can be on either side of the object plane.)

The diffractive image will be affected by chromatic aberration, but the chromatic effects can be substantially neutralized by a diffractive projection mirror or mirrors in the same manner as the maskless design. Also, either the microlenses in a maskless system or the photomask in a holographic mask-projection system can control the phase of the diffracted radiation to offset and neutralize geometric optical aberrations in the projection system. Thus, the microlenses or holographic mask operate in combination with the diffractive mirror or mirrors to substantially neutralize both geometric and chromatic aberrations.

DESCRIPTION

Maskless EUV lithography scanner

FIG. 1 shows a schematic cross-sectional view of a maskless EUV lithography scanner. An LPP plasma **101** generates EUV radiation, which is focused by an ellipsoidal collection mirror **102** to an intermediate focus IF, where it is spatially filtered by a small aperture **103**. (A portion **104** of the LPP power may be diverted to one or more other similar scanner modules.) The IF-transmitted radiation is directed by illumination optics comprising two illumination mirrors, grazing-incidence element **105** and near-normal-incidence element **106**, onto microlens array **107**. (Many alternative

design forms for the illumination optics are possible.) The microlenses partition the radiation into a large number of individual convergent beams (e.g., approximately 2 million). A projection system comprising two axially-symmetric, annular mirrors M1 and M2 focuses the beams onto an array of diffraction-limited focal spots on a writing surface **108** at the projection system's image plane. (The projection mirrors are a variant of the a flat-image Schwarzschild design, Ref. 10, adapted to operate at finite conjugate.) The beams are individually modulated as the surface **108** is scanned across the spot array to synthesize a digital, high-resolution raster image.

FIG. 2 schematically illustrates the scan process. The focal spot array **201** writes a raster line pattern as the writing surface **108** scans from left to right in the figure. For example, spot **202** writes line **203**. Practical variations of the scan process are described in detail in Ref's. 1 and 2.

FIG. 3 shows an enlarged cross section of the microlens array **107** in FIG. 1, which is formed as a structured, topographic pattern layer **301** on a transparent substrate **302**, supported by a microchannel plate **303**. (The microchannel plate will probably need to be made from Zerodur for thermal stability. Ref. 17.) Each microlens, such as element **304**, focuses illumination into a beam converging toward and through a focal point **305** on the projection system's object plane **306**. (Illustrative dimensions are 15 microns for the lens diameter and 81 microns for the lens focal length and plate thickness.) Conical holes are formed in the plate to accommodate the beam paths. An array of small apertures at the focal plane, such as aperture **307**, can be used to spatially filter the focused beams.

Micromechanical shutters, such as shutter **308**, modulate the beams at or near the focal points in synchronization with the LPP pulse rate. Alternatively, the shutters can be omitted and the beams can be collectively modulated at the LPP source (e.g., by modulating the LPP drive laser intensity or targeting). A source-modulated scanner would be limited to printing periodic patterns matching the focus spot periodicity on the writing surface.

Micromechanical shutters would typically have a travel range of order 0.1 micron, whereas a source-modulated scanner would require a single shutter covering an aperture dimension of order 100 microns. High-speed (e.g., >100 kHz) beam modulation of a beam of such size could be achieved by arraying multiple MEMS-actuated, long-stroke shutters around the periphery of a spinning disc, which intercepts an EUV beam at the LPP source's intermediate focus. For example, one thousand shutters arrayed along the edge of a disc of circumference 100 mm, each

modulator of size 100 micron and operating at a 1 kHz switching rate, could collectively modulate the beam at a 1 MHz rate.

Microlens element **304** is illustrated in FIG. 4A in cross-section, and in FIG. 4B in plan view. An expanded cross-sectional view of the diffractive lens profile is illustrated in FIG. 5, and FIGS. 6 and 7 show two alternative designs. The profile geometry is similar to a diffraction grating. FIG. 5 shows a binary zone-plate lens profile; FIG. 6 shows a linear-ramp, blazed lens profile; and FIG. 7 shows a stepped, multi-level blazed lens profile. (Two levels are illustrated in FIG. 7, but higher optical efficiency could be obtained with more levels.) Blazed lenses (FIG. 6 or 7) would be preferred for high efficiency, but conventional binary zone-plate lenses (FIG. 5) can be more easily manufactured. Each lens comprises a pattern of concentric, annular phase zones (annular line-space pairs), such as zone **501**, formed by etching a phase-shift topographic pattern into layer **301** on the substrate **302**. In the illustrative design there are approximately 24 phase zones (FIG. 4B), and the minimum zone width (grating period) is approximately 1% of the lens diameter (e.g., 150 nm width for a 15-micron diameter).

For a 13.5-nm operating wavelength the phase-shift layer **301** would typically be molybdenum (Mo) and the substrate **302** could be silicon (Si). The profile depth (Mo layer thickness) would typically be approximately 85 nm for a binary lens (FIG. 5), or somewhat higher for a blazed lens; and the Si substrate could be approximately 50- to 100-nm thick. (Practical fabrication details for these types of lenses are discussed in Ref. 5.) For a 6.7-nm operating wavelength, the phase-shift layer could be lanthanum (La), approximately 200-nm thick for a binary lens, and the substrate could be boron carbide (B₄C), approximately 100- to 200-nm thick. The phase-shift layer could alternatively be a lanthanum compound such as lanthanum nitride (LaN) or lanthanum carbide (LaC₂).

The lens aperture can be circular in FIG. 4B, but the annular phase zones are slightly elliptical and distorted to compensate for optical aberration (e.g., astigmatism) in the projection system. The focused beam is significantly aberrated at focal point **305** (FIG. 3), but the lens **304** generates an optical wavefront that emerges from the projection system as a substantially aberration-free, spherical, point-convergent wave. (The spatial filter apertures such as aperture **307** can be underfilled to avoid interfering with the aberration correction function.)

The lenses can achieve substantially perfect aberration correction at a particular design wavelength, but singlet lenses will exhibit significant chromatic aberration over the operating

wavelength range. (A diffractive lens operates in a manner similar to a diffraction grating, which is chromatically dispersive.) Rather than using an achromatic doublet lens, as in '983 and Ref's. 1 and 2, the chromatic aberration is corrected by using a diffractive projection mirror M2, which is illustrated schematically in cross-section in FIG. 8A and in plan view in FIG. 8B. The mirror surface comprises annular, concentric phase zones, depicted schematically as concentric circles in FIG. 8B. An illustrative mirror diameter is 600 mm, and the number of phase zones is approximately the same as the microlenses, e.g. 24, as illustrated. These conditions imply a minimum zone width of approximately 6 mm on M2.

The mirror phase zones induce an optical phase shift in the reflected radiation in a manner similar to a diffraction grating. The zone structure is blazed to substantially concentrate the diffracted light into a single diffraction order, and the chromatic aberration induced by the diffractive mirror substantially offsets and neutralizes that of the diffractive microlenses. (The chromatic correction is not perfect because the mirror is constrained to being axially symmetric. But it can reduce the chromatic aberration to a level that may be substantially negligible.)

An expanded cross-sectional view of the diffractive mirror structure in FIG. 8A is illustrated in FIG. 9. A conventional EUV mirror reflection coating, e.g. for a 13.5-nm operating wavelength, is first constructed by depositing alternate layers of Mo and Si on the mirror substrate, with a typical Mo/Si bilayer thickness in the range of 7 to 10 nm. (One bilayer is indicated as **901**.) The total number of deposited bilayers would typically be around 70 or more. An ion-beam finishing (IBF) process is then applied to the multilayer stack to ion-mill a bowl-shaped depression traversing the layers, and a protective top coat (e.g. a couple nanometers of Si or ruthenium) is then deposited to prevent oxidation of the Mo. The phase zones are demarked by the intersections of the bilayer boundaries with the IBF-processed top surface (e.g. zone **902** is demarked by bilayer **901** boundaries).

IBF processes are routinely used in optical manufacturing, e.g. with IBF tools manufactured by Buhler, a company based in Switzerland. Similar processes have been applied to EUV mirrors. U.S. Patent 7,050,237 (hereafter '237) discloses an EUV multilayer cut at a shallow angle, which has "the same properties as a blazed grating, and has been demonstrated to have near-perfect performance." The cut is made either by mechanical or ion-beam polishing (similar to IBF). Either method could be applied to manufacture chromatic dispersion-compensating mirrors of the form illustrated in FIG. 9. FIG. 3 in '237 illustrates an ion-beam polishing process using a broad-

area ion beam and a movable mask. (The Buhler IBF systems do not require masking; they raster-scan a small-area ion beam across the workpiece to form the desired surface shape.)

The diffractive structures disclosed in '237 require thousands of Mo/Si bilayers to form a grating of significant area. By contrast, the dispersion-compensating mirror of FIG. 8A and 8B requires relatively few bilayers. The number of bilayers that are cut by the IBF process is equal to the number of diffractive phase zones on the mirror, e.g., about 24 as illustrated in FIG. 8B.

Tsuru (Ref. 11) also discloses ion milling of EUV multilayer mirrors, in this case for the purpose of correcting mirror figure errors to the 0.1-nm level. (This application is unrelated to chromatic dispersion.)

The diffractive mirror structure can alternatively be formed by a selective deposition process. Mo/Si layers are typically deposited using magnetron sputtering, and a mask could be placed proximate to or in contact with the mirror surface during deposition of each layer to delimit the deposition area. (Even with conventional, non-diffractive EUV mirrors some form of deposition masking is typically required to control the Mo/Si layer thickness distribution across the mirror aperture.) Masking processes, either with ion-beam polishing or deposition, could result in a diffractive structure with discontinuous zone boundaries as illustrated in FIG. 10.

There are other alternative approaches that can also be used for manufacturing diffractive EUV mirrors. For example, a blazed profile structure with a typical depth in the range of 7 to 10 nm can be formed in the mirror substrate (e.g., via grayscale lithography), after which a multilayer Mo/Si reflection coating is conformally deposited on the substrate. (Structures of this type are illustrated, for example, in Ref. 12.)

The illustrative mirror materials and dimensions discussed above are applicable to a 13.5-nm operating wavelength. For a 6.7-nm wavelength, Mo and Si would be replaced by materials such as La (or a La compound such as LaN or LaC₂) and B₄C (Ref. 4) and the bilayer thicknesses would be reduced by about a factor of 2. These materials have relatively low refractive index contrast, so many more bilayers (e.g. ~200) would be required to achieve high reflectivity, and the mirror reflection bandwidth at wavelength 6.7 nm will be much narrower than a Mo/Si mirror at wavelength 13.5 nm. Due to the narrower bandwidth, it might be possible to operate the system without chromatic aberration compensation, in which case a diffractive projection mirror (or achromatic microlenses) would not be required.

Similar dispersion-compensating mirrors could be used for visible-light, UV, or DUV systems. The mirror could use a multilayer-dielectric reflection coating analogous to EUV Mo/Si coatings. Alternatively, an aluminum reflection coating could be conformally deposited on a blazed substrate structure (similar to spectrometer reflection gratings).

Diffractive mirrors formed by the above-described IBF process (similar to FIG. 9 or FIG. 10) could also be used for general-purpose optical systems requiring diffractive mirrors – either for EUV or for visible, UV, or DUV wavelengths.

Holographic mask-projection lithography

Referring back to FIG. 3, the microchannel plate **303** and spatial-filter apertures **307** would not be needed for stray light suppression and could be eliminated if the microlenses are blazed (as in FIG. 6 or 7) to suppress optical scatter from extraneous diffraction orders within the projection system's angular acceptance range (the range of diffraction directions entering the projection system, FIG. 1). This would leave a microlens array **107** on a thin, edge-supported substrate **302**, as illustrated schematically in FIG. 11. (The illumination **1101** and convergent beams are depicted as shaded areas in FIG. 11.) But in this configuration the pattern need not have the form of a microlens array. Any kind of diffractive structure can be used to form an arbitrary full-field image, not just a point-array image. Thus, the microlens array can be transformed into a transmission mask and the same optical system (FIG. 1) can be used for mask-projection (not maskless) lithography. For example, FIG. 12A schematically illustrates a mask **1201** comprising a portion **1202** that focuses illumination to an isolated point **1203** on the object plane **306** in the same manner as a microlens in a maskless system. Another portion **1204** of the mask has the form of a diffraction grating, which creates a dense line/space pattern via interference between the grating's plus-first and minus-first diffraction orders. The interference pattern between intersecting diffraction orders is illustrated as the banded area **1205**, indicating areas of constructive and destructive interference. (This is basically a small-scale implementation of interference lithography, Ref. 13.) Other types of structures can be used to form a variety of image patterns.

Unlike the microlens array of a maskless scanner, the transmission mask in FIG. 12A is not supported on a Zerodur microchannel plate and will be sensitive to thermal expansion, e.g. resulting from EUV irradiation. The mask can be supported by a tensioned frame with capacitive

or optical interferometric sensors to detect the expansion, and active radiant heating (e.g. with visible-light radiation) can be applied to control the expansion in response to sensor feedback.

Alternatively, if the exposure image consists of area-limited structures created by non-overlapping mask patterns (such as patterns **1202** and **1204** in FIG. 12A), then the mask could be formed on a supporting plate, similar to microchannel plate **303** in FIG. 3, with hollow channels or windows for beam transmission. For example, FIG. 12B illustrates a variation of the FIG. 12A structure with a backing plate **1206** providing structural support.

In the mask-projection operational mode the illumination need not be modulated and the pattern is not scanned; it is statically projected onto the writing surface to expose a full image field, and larger fields of unlimited size are exposed via field stepping and stitching. (A standard-size mask can accommodate separate patterns for multiple exposure fields, so the stitching process would not necessarily require any mask changes.) Writing throughput would not be limited by any modulator frame rate or by the LPP source repetition rate, so mask-projection lithography could achieve higher throughput than maskless lithography.

This form of mask-projection lithography is “holographic” because the mask **1201** (a holographic mask) is not imaged directly onto the writing surface; it rather forms a diffractive (holographic) image on the projection system’s object plane **306** some distance from the mask, and that intermediate image is projected onto the writing surface. The object plane can be on either side of the mask. In FIG. 12A it follows the mask in the optical path; FIG. 13 illustrates an alternative design in which it precedes the mask.

Alternatively, a holographic mask could be used in a scanning mode similar to maskless lithography, in which the writing surface is continuously scanned across the image field while it is being exposed. This mode of operation could be used, e.g., for printing extended lines or blanket area exposures. A holographic mask would provide more flexibility than maskless lithography with a microlens array because the exposure pattern need not be limited to a periodic point array.

Holographic lithography, like maskless, can correct projection system aberrations and image distortion. The optical pattern on the writing surface can be viewed as an integral superposition of point images, each of which is generated by a point-convergent spherical wave originating from the mask. The wave shape is generally not exactly spherical in the vicinity of the mask; it has a shape determined so that after passing through the projection system the wave emerges as a spherical, point-convergent wave. With broadband illumination the wave shapes will

be wavelength-dependent, leading to chromatic aberration, but the chromatic effects can be substantially neutralized with a diffractive projection mirror or mirrors in the same manner as maskless lithography (FIGS. 8A-10).

In comparison to conventional mask-projection lithography in which the mask is located at the object plane, holographic lithography would tend to be less sensitive to isolated mask defects because the defects are not in focus at the image plane. In addition, holographic lithography could achieve much higher exposure dose levels, especially for isolated patterns, because it operates by diffractively focusing, rather than absorbing (“masking”) the illumination. For example, a conventional mask would produce an isolated point image by forming a very small transmittance window on an opaque mask layer, whereas a holographic mask could focus illumination from a much larger illumination area onto the point.

Holographic lithography would typically operate as a “step-and-repeat” system in which the mask and writing surface are substantially stationary during image exposure, in contrast to conventional mask-projection scanners in which the mask and writing surface are concurrently scanned across the illumination field. The fixed positional relationship between the holographic mask and the projection system makes it possible for the mask to correct projection system aberrations, and accurate alignment of the system components can be more easily maintained when the elements are stationary. (But as noted previously, the writing surface could alternatively be continuously scanned during exposure.)

An isolated image point in a holographic lithography system is basically a diffraction-limited image of the source. The LPP source would need to be sufficiently compact, or should be spatially filtered by a sufficiently small IF aperture **103** (FIG. 1), to achieve diffraction-limited source imaging. Also, diffraction-limited imaging necessitates illumination optics between the IF and mask that provide illumination with minimal angular spread at each mask point. A holographic stepper uses full-field illumination optics, which facilitate diffraction-limited source imaging. Conventional EUV scanners generally use dispersive illumination optics and ring-field illumination, which would not be useful for holographic lithography because they would not produce a well-resolved source image.

A holographic mask-projection stepper will spend a significant amount of time stepping between exposure fields and performing pre-exposure alignment operations. The writing surface is repositioned between exposures, and if the image pattern is changed then the mask is also

repositioned or replaced with a different mask. This could leave the LPP source idle during field stepping. However, source utilization can be maximized by switching the illumination beam between two or more or stepper modules so that one module can be exposing an image while the other modules are being stepped. Beam switching can be effected by a movable mirror or diffraction grating in the beam path near the intermediate focus. For example, FIGS. 14A and 14B illustrate a beam-switching mechanism comprising two EUV beam-deflection mirrors **1401** and **1402** proximate the IF, which are translationally moved to effect beam switching between two optical paths **1403** and **1404**. A translationally actuated diffraction grating or gratings (either transmission or reflection gratings) could be alternatively used in lieu of mirrors.

FIGS. 15A-D illustrate an alternative beam-switching mechanism comprising a rotating disk **1501** with an EUV-transmission diffraction grating (e.g. a Mo phase-shift pattern on a thin Si substrate) formed over an annular aperture **1502** near the edge of the disk. The disk is illustrated in perspective view in FIGS. 15A and 15B, and in plan view in FIG. 15C. The grating aperture is divided into two or more subapertures (e.g. subapertures **1503** and **1504**) and the grating structure in each subaperture is configured so that the diffracted beam does not move while the beam intercepts the moving subaperture. For example, the grating can comprise radial zones such as zone **1505**. The two subapertures effect beam switching by deflecting the beam in different directions. FIGS. 15A and 15B illustrate two beam directions **1506** and **1507**. The two subapertures could, for example, be constructed as blazed transmission gratings with similar zone geometries, but with opposite blaze orientations, as illustrated by the cross-sectional view in FIG. 15D. The sawtooth structure represents the blazed grating facets, such as facet **1508** on zone **1505**. The grating substrate could alternatively be conical, cylindrical, or any cylindrically symmetric shape. Also, a reflection grating could alternatively be used in lieu of a transmission grating. The beam-switching grating might induce some optical aberration in the transmitted beam, which can be corrected in the illumination optics (e.g., mirrors **105** and **106** in FIG. 1).

The optical design of a holographic mask can be simplified by incorporating a zero-order stop in the projection optics of FIG. 1. As illustrated in FIG. 16, the annular mirror M1 and M2 apertures create a central obscuration zone (i.e., a shadow region) in which a zero-order stop (blocking mask) **1601** can be inserted. (The stop can be supported by either spider vanes, tension wires, or a pellicle crossing the optical path, not shown.) This simplifies the mask design because there is no need for zero-order extinction. For example, portions of the mask that are intended to produce a dark (zero-intensity) image can simply be unpatterned; there is no need for an absorber

or diffractive extinction of the zero order. The system operates in darkfield imaging mode. If a bright field is needed (e.g. for flood exposure or area fill) then a blazed phase grating can be formed on the mask to direct radiation outside of the obscuration zone. An area-fill exposure pattern can also be made by doing two exposures of a two-beam interference pattern (such as pattern **1205** in FIG. 12A) with the writing surface displaced by half of the image period between exposures. Alternatively, an isolated line image can be scanned to cover an extended area.

As illustrated in FIG. 17, the zero-order stop can alternatively be replaced with a small mirror **1701**, which directs illumination **1702** onto a reflective holographic mask **1703** (rather than a transmission mask). The mirror **1701** performs a dual function of providing illumination to the mask and operating as a zero-order stop. The holographic mask is illuminated at near-normal incidence, so it would exhibit minimal 3-D effects compared to conventional EUV masks, which are illuminated at oblique incidence.

A holographic mask, and the mask illumination optics, can be constructed to cover an image aperture with a shape such as a rectangle or hexagon that can be periodically tiled over the writing surface. For example, FIG. 18 illustrates a hexagonal illumination field **1801** (shaded area) on the writing surface **108**. The illumination covers a hexagonal aperture **1802** whose perimeter defines “stitch lines” for pattern stepping, and the illumination can be apodized (tapered) across the stitch lines to avoid edge diffraction effects. Successive exposures are made with the writing surface stepped so that the stitch lines of adjacent illumination fields are aligned and apodized edges are overlapped, as illustrated in FIG. 19. FIG. 20 illustrates a holographic mask **2001**, in plan view, which has multiple exposure patterns such as pattern **2002**. The pattern images can be stitched via field stepping to seamlessly cover an extended print area, and multiple masks can be used to cover an even larger contiguous print area.

Mathematical description of optical systems

An engineering specification of the above-described lithography systems requires a mathematical framework based on a physical optics foundation, as outlined below. Numbered equations are tabulated in FIG. 21.

The propagation of electromagnetic radiation through an optical system is generally modeled using a combination of near-field diffraction modeling and geometric optics. Near-field modeling applies to electromagnetic interaction with matter on wavelength-scale or smaller

dimensions, e.g. within a multilayer reflection coating or in a diffraction grating, and requires accurate electromagnetic simulation, e.g. via Rigorous Coupled-Wave Diffraction theory (RCWA, Ref. 14). Geometric optics applies to propagation of optical waves through homogeneous media (e.g. vacuum) over distances much longer than the wavelength.

In the context of geometric optics a monochromatic electromagnetic field is characterized by “geometric waves”, loci of constant optical phase, which propagate according the laws of geometric optics. The optical phase, measured in cycle units (aka “waves”; 1 cycle = 2π radian), is denoted as p . The phase gradient ∇p has magnitude $1/\lambda$ in vacuum (Eq. **21.1**), where λ is the wavelength. This is the “Eikonal equation” upon which geometric optics is based. Optical rays are straight lines orthogonal to the geometric waves (i.e., parallel to ∇p), and p varies by one phase cycle per wave along an optical ray. The ray direction at any particular point on the ray is defined by a direction vector $\hat{\mathbf{u}}$, comprising direction-cosine coordinates, which is the phase gradient times the wavelength, Eq. **21.2**. The Eikonal equation implies that $\hat{\mathbf{u}}$ is a unit vector, Eq. **21.3**.

The total electromagnetic field in a region of space (e.g. within a lithography system’s projection optics) can comprise a multiplicity of overlapping geometric-optic fields. The multiplicity can be an infinite continuum, i.e. an integral superposition of geometric-optic fields. The total field can typically be represented equivalently with alternative continuum descriptions, e.g. as a superposition of plane waves or as a superposition of point-convergent, spherical waves associated with image points.

It follows from the Eikonal equation that a geometric-optics field’s complete three-dimensional phase distribution can be constructed from its phase on a particular surface traversed by the field, by the following procedure: Given a specification of p on the surface, the surface-tangential projection of its gradient ∇p is determined, and the surface-tangential projection of the ray direction vector $\hat{\mathbf{u}}$, denoted as $T\hat{\mathbf{u}}$, is determined from Eq. **21.2**. The vector’s surface-normal component, denoted as $N\hat{\mathbf{u}}$, is determined from the conditions that $N\hat{\mathbf{u}}$ is orthogonal to the surface and $|\hat{\mathbf{u}}|$ is equal to 1. (The sign of $N\hat{\mathbf{u}}$ is undetermined by these conditions, but is defined based on which side of the surface the field is propagating into.) The relationships between $\hat{\mathbf{u}}$, $T\hat{\mathbf{u}}$, and $N\hat{\mathbf{u}}$ are described in Eq’s. **21.4** and illustrated in FIG. 22, in which $\hat{\mathbf{s}}$ denotes the surface-normal unit vector at any particular surface point. Once $T\hat{\mathbf{u}}$ and $N\hat{\mathbf{u}}$ are known at the point, the optical ray

direction vector $\hat{\mathbf{u}}$ at that point is determined and the phase along the ray is determined by the condition that the phase varies by one cycle per wave along the ray.

The geometric theory of reflection at an optical surface is generally derived assuming a planar mirror and plane-wave illumination, but is applicable to curved mirrors and waves if the curvature is not significant over wavelength-scale dimensions. For reflection at a bare, uncoated mirror surface, the phase of a reflected beam is determined by the conditions that its phase is equal to that of the incident beam on the reflecting surface (except for a constant phase shift), implying that $T\hat{\mathbf{u}}$ is unchanged by reflection, and $\hat{\mathbf{s}} \cdot \hat{\mathbf{u}}$ changes sign upon reflection.

Optical ray trace programs typically model mirrors as infinitesimally thin reflective surfaces, but in the case of EUV the reflection does not occur at a discrete surface; the reflection is distributed through a multilayer film many wavelengths thick. Nevertheless, the mirror can be modeled as a discrete surface by the following procedure. FIG. 23 illustrates a cross-sectional view of the multilayer reflective film **2301**. A reference reflection surface **2302** near or within the film is defined; the incident field **2303** (depicted schematically as a wave train) is defined, and an accurate near-field electromagnetic calculation is performed to calculate the local reflected field **2304** in the vicinity of each point on the reference surface. (This calculation can be done using flat-surface and plane-wave approximations.) The incident and reflected fields outside of the mirror coating are analytically extrapolated to the reference surface **2302**, and their phase difference on the surface is calculated. Standard ray tracing procedures can be applied, using reference surface **2302** as the effective mirror surface, but with the calculated phase offset applied to the reflected field.

Diffraction lenses and mirrors can similarly be modeled using a combination of near-field and geometric-optic calculation methods. Accurate near-field diffraction models such as RCWA assume a flat grating with periodic phase zones and plane-wave illumination, but approximations based on these conditions can be used to calculate local diffraction characteristics of diffractive lenses and mirrors with non-flat substrates, aperiodic phase zones, and non-planar waves.

Geometric ray tracing methods typically represent a diffractive element as an infinitesimally thin surface characterized by a “grating phase” gp , a continuous function of position on the surface, which varies by one unit per phase zone. (The zone boundaries can be defined as the loci on which gp takes on integer values.) A geometric-optics incident field will generally be diffracted into multiple diffraction orders, and the optical phase p'_m of the m -th

diffraction order on the surface ($m = \dots, -1, 0, 1, \dots$) will differ from the incident field phase p_0 by m times gp , Eq. 21.5. Based on this condition and Eq. 21.2, the incident and diffracted ray direction vectors, denoted as $\hat{\mathbf{u}}_0$ and $\hat{\mathbf{u}}'_m$, have surface-tangential projections $T\hat{\mathbf{u}}_0$ and $T\hat{\mathbf{u}}'_m$, which are related to the surface-tangential grating phase gradient $T\nabla gp$ by Eq. 21.6. The surface-normal projections are determined from the surface-tangential projections as described above (Eq's. 21.4 and FIG. 22).

As in the case of a multilayer mirror, a diffractive structure with significant depth, such as a zone-plate lens or IBF-processed mirror, can be modeled in ray trace calculations as an infinitesimally thin diffracting element, which induces a small additional phase shift to account for 3-D near-field diffraction effects within the structure. A near-field simulation method such as RCWA can be used to calculate the corrective phase shift.

Optical design for the projection system

FIG. 24 tabulates illustrative design data for a Schwarzschild projection system similar to FIG. 1. FIG. 25 illustrates the mirror geometry, which is referenced to (x_1, x_2, x_3) Cartesian coordinates and is axially symmetric around an optical axis **2501** coinciding with the x_1 axis. The coordinate origin is at the image plane **2502** and x_1 is downward-positive (in the object-to-image direction). The illumination optics (not shown) focus EUV illumination toward a source focal point **2503** on the optical axis at coordinate location $x_1 = \text{Src_x1}$ below the image plane. (For the purpose of design specification, the source is treated as a single point at the IF in FIG. 1, which is imaged by the illumination optics to point **2503**.) A portion of FIG. 25 is expanded in FIG. 26 (similar to FIG. 3), showing the relationship between the microlens array **107** plane (or holographic mask plane), at coordinate location $x_1 = \text{Lens_x1}$, and the projection system's object plane **306** at $x_1 = \text{Object_x1}$. The mirror M1 and M2 shape functions intercept the axis **2501** at $x_1 = \text{M1_x1}$ and $x_1 = \text{M2_x1}$, respectively. Each mirror shape is defined by a "superconic" function of the form defined in Eq. 21.7 in FIG. 21, in which M_x1 is either M1_x1 or M2_x1 and the coefficients c_1, c_2, \dots have the values tabulated in FIG. 24 for each mirror. The M2 grating phase gp has the function form defined in Eq. 21.8, with coefficients pc_1 and pc_2 also tabulated in FIG. 24.

The microlenses' grating phase functions are defined to achieve zero-aberration imaging of the source center point at the image plane, and at the 13.5-nm design wavelength. This can be achieved by applying a phase-matching process: Rays from an image point corresponding to any particular lens are reverse-traced from the point back through the projection optics and onto the lens. The ray-trace procedure defines the transmitted optical phase at each ray intercept on the lens (at wavelength 13.5 nm), and the point-convergent source field's incident optical phase at the same intercept point is subtracted from the transmitted phase to define the grating phase at that point. This construction follows from Eq. 21.5 in FIG 25, with p_0 representing the incident beam's phase, p'_m representing the transmitted beam's phase in diffraction order m (typically $m = 1$), and with gp representing the lens's grating phase. The surface-tangential gradient of the grating phase, $T\nabla gp$, is determined from Eq. 21.6. Once gp and $T\nabla gp$ are determined, Eq's. 21.5 and 21.6 can then be used to perform geometric ray tracing for other wavelengths and source points.

In developing the above-outlined design, the diffractive and reflective surfaces were approximated as infinitesimally thin layers. In practice, small surface phase offsets would need to be applied, as described in the preceding section, to account for the 3-D depth of the diffractive and reflective structures.

The design data in FIG. 24 was determined through an optical optimization procedure, using a merit function of the form defined by Eq. 1 in Ref. 2. The design numerical aperture (NA) is 0.55 (the same as ASML's EXE-5000 system), but the optimization was done using an oversized NA of 0.61 to preserve circularity of the microlens apertures and to avoid steep gradients in the grating phase at the lens periphery. The inner (obscuration) numerical aperture, NA_{inner} , is 0.125, implying a 5% aerial obscuration ratio: $(0.125 / 0.55)^2 = 0.052$. The demagnification factor, $demag$, is 6.

The calculated optical phase aberration of the projection system at the edge of the image field (where the aberration is highest) is 1-wave RMS (root-mean-square) and 4-wave P-V (peak-valley) at wavelength 13.5 nm, without correction by the microlenses. With the correction, the worst-case phase error is reduced to 0.01-wave RMS and 0.05-wave P-V over the wavelength range 13.35-13.65 nm and across a circular image field of diameter 7.8 nm defined by the source's geometric image on the writing surface. (The 7.8-nm source image size is based on Ref. 2.)

Holographic mask structure

FIG. 27 shows a cross-sectional schematic of a reflective holographic mask **2701**, which is functionally similar to portion **1204** of the transmission mask **1201** illustrated in FIG. 12A. A diffractive structure on the mask reflects incident illumination **2702** into two diffracted beams **2703** and **2704** (+1 and -1 diffraction orders), which intersect to form a line/space interference pattern at the object plane **306**. (The pattern can be pre-distorted and aberrated to correct the projection system's distortion and aberrations.) The central portion **2705** of the structure operates as a beam splitter, dividing the reflected radiation into two diffracted beams. Each outer portion **2706** and **2707** only generates one diffraction order. (However, all three portions can reflect some of the radiation into an undiffracted zero order, which is blocked by the mirror **1701** in FIG. 17, and they can also divert some radiation into high diffraction orders outside of the projection system's angular acceptance range.)

FIG. 28 shows a possible structure for the center beam-splitting portion **2705**, in a cross-sectional view. The structure comprises ruthenium (Ru) grating lines such as line **2801** (shown in cross-section) and Si-filled spaces such as space **2802** formed on a Mo/Si multilayer reflective coating **2803**. (There would typically be 40 or more Mo/Si bilayers.) Illustrative dimensions are $t_1 = 33.0$ nm for the line thickness, $w_1 = 108.6$ nm for the Ru linewidth, and $\Lambda = 200$ nm for the grating period. (There would typically be many more periods than the two illustrated.) Normally incident EUV illumination at wavelength 13.5 nm is reflected into +1 and -1 diffraction orders (**2703** and **2704** in FIG. 27), each with 18.7% diffraction efficiency. About 1.7% of the incident power is reflected into the zero order, which is blocked in the projection optics (by mirror **1701** in FIG. 17). Other diffraction orders are outside of the projection system's angular acceptance range. The grating period, 200 nm, will result in an interference pattern with a 100-nm period on the object plane, which is imaged by the projection optics, e.g. at 6X reduction, to a periodic line/space pattern with 16.7-nm period on the writing surface.

The side portion of the pattern, **2706** in FIG. 27, could have the structure illustrated in FIG. 29. This structure also comprises Ru grating lines such as line **2901** and Si-filled spaces such as space **2902** formed on the same Mo/Si reflective coating **2803**, and with the same 33-nm thickness (t_1) and 200-nm period (Λ) as the center portion, but with a narrower Ru line width ($w'_1 = 73.3$ nm in FIG. 29 versus $w_1 = 108.6$ nm in FIG. 28). In addition, a second Ru layer **2903** of thickness $t_2 = 16.2$ nm is deposited on the structure and is patterned to form a grating with the same 200-nm

period and with linewidth $w_2 = 148.5$ nm. (There is no Si fill in this grating's spaces. The top and bottom Ru grating lines' left edges are aligned.) This structure diffracts 18.7% of the illumination power into the +1 diffraction order **2703** in FIG. 27 (matching the efficiency of the FIG. 28 structure) and has substantially zero power in the -1 order **2704**. (Much of the remaining power is shunted to the zero order, which has efficiency 9.2%.) The lateral displacement between the FIG. 28 and FIG. 29 structures is determined to achieve phase matching in the +1 diffraction order. Side portion **2707** in FIG. 27 can have a structure similar to FIG. 29, but configured to concentrate the reflected radiation in the -1 order rather than the +1 order.

Mask designs such as FIGS. 28 and 29 can be developed using near-field diffraction simulation tools such as RCWA, Ref. 14. Data on the optical characteristics (complex refractive index) of EUV materials can be obtained from the CXRO database, Ref. 15. More general holographic mask structures can comprise any number of layers with two or more line edges per period, or the structures can be topographically contoured (e.g. via grayscale lithography) rather than layered. They can also be aperiodic (e.g. for isolated image patterns), and three-dimensional structures such as checkerboard phase-shift gratings (similar to those described in Ref. 16) can be used to produce exposure patterns other than parallel lines and spaces.

References

The following additional patent and literature references are referred to in this disclosure and are incorporated by reference:

U.S. Patent No. 9,097,983	issued August 2015	Johnson
U.S. Patent 7,499,149	issued March 2009	Hendriks et al.
U.S. Patent 7,050,237	issued May 2006	Chapman

Ref. 1: K. Johnson, "Maskless EUV Lithography", presented at the 2019 EUVL Workshop.
<https://www.euvlitho.com/2019/P22.pdf>

Ref. 2: Kenneth C. Johnson, "Maskless EUV lithography, an alternative to e-beam," *J. Micro/Nanolith. MEMS MOEMS* 18(4), 043501 (2019)
<https://doi.org/10.1117/1.JMM.18.4.043501>

Ref. 3: Erdmann, Andreas, et al. "3D mask effects in high NA EUV imaging." *Extreme Ultraviolet (EUV) Lithography X*. Vol. 10957. International Society for Optics and Photonics, 2019.

<https://doi.org/10.1117/12.2515678>

Ref. 4: P. Naujok et al., "B-based ML coatings for Blue-X", presented at the 2019 EUV Source Workshop.

<https://www.euvlitho.com/2019/S23.pdf>

Ref. 5: Salmassi, Farhad H., et al. "Fabrication and performance of transmission engineered molybdenum-rich phase structures in the EUV regime (Conference Presentation)." *International Conference on Extreme Ultraviolet Lithography 2017*. Vol. 10450. International Society for Optics and Photonics, 2017.

<https://doi.org/10.1117/12.2281487>

Ref. 6: Deuter, V., et al. "Holographic masks for computational proximity lithography with EUV radiation." *International Conference on Extreme Ultraviolet Lithography 2018*. Vol. 10809.

International Society for Optics and Photonics, 2018.

<https://doi.org/10.1117/12.2502879>

Ref. 7: Cheng, Yang-Chun, et al. "Extreme ultraviolet holographic lithography: Initial results." *Applied Physics Letters* 90.2 (2007): 023116.

<https://doi.org/10.1063/1.2430774>

Ref. 8: Isoyan, A., et al. "Extreme ultraviolet holographic lithography with a table-top laser." *Alternative Lithographic Technologies*. Vol. 7271. International Society for Optics and Photonics, 2009.

<https://doi.org/10.1117/12.814678>

Ref. 9: Borisov, Michael V., et al. "Experimental verification of sub-wavelength holographic lithography physical concept for single exposure fabrication of complex structures on planar and nonplanar surfaces." *33rd European Mask and Lithography Conference*. Vol. 10446. International Society for Optics and Photonics, 2017.

<https://doi.org/10.1117/12.2279736>

Ref. 10: Bass, Michael. *Handbook of Optics Volume II Devices, Measurements, and Properties*. McGraw-Hill, Inc., 1995. (p. 18.15)

Ref. 11: Tsuru, T., K. Arai, and T. Hatano. "Homogenized ion milling over the whole area of EUV spherical multilayer mirrors for reflection phase error correction." *Journal of Physics. Conference Series (Online)*. Vol. 425. No. 15. 2013.

<https://doi.org/10.1088/1742-6596/425/15/152009>

Ref. 12: Voronov, D. L., et al. "Enhancement of diffraction efficiency via higher-order operation of a multilayer blazed grating." *Optics Letters* 39.11 (2014): 3157-3160.

<https://doi.org/10.1364/OL.39.003157>

Ref. 13: Päivänranta, Birgit, et al. "Sub-10 nm patterning using EUV interference lithography." *Nanotechnology* 22.37 (2011): 375302.

<https://doi.org/10.1088/0957-4484/22/37/375302>

Ref. 14: Kenneth C. Johnson (2019) Grating Diffraction Calculator (GD-Calc ®) [Source Code].

<https://doi.org/10.24433/CO.7479617.v3>

Ref. 15: The Center for X-Ray Optics, Lawrence Berkeley National Laboratory, "CXRO X-Ray Interactions With Matter."

http://henke.lbl.gov/optical_constants/

Ref. 16: Naulleau, Patrick, et al. "Ultrahigh efficiency EUV contact-hole printing with chromeless phase shift mask." *Photomask Japan 2016: XXIII Symposium on Photomask and Next-Generation Lithography Mask Technology*. Vol. 9984. International Society for Optics and Photonics, 2016.

<https://doi.org/10.1117/12.2243321>

Ref. 17: Weigel, C., Schulze, M., Gargouri, H., & Hoffmann, M. (2018). "Deep etching of Zerodur glass ceramics in a fluorine-based plasma." *Microelectronic Engineering*, 185, 1-8.

<https://doi.org/10.1016/j.mee.2017.10.013>

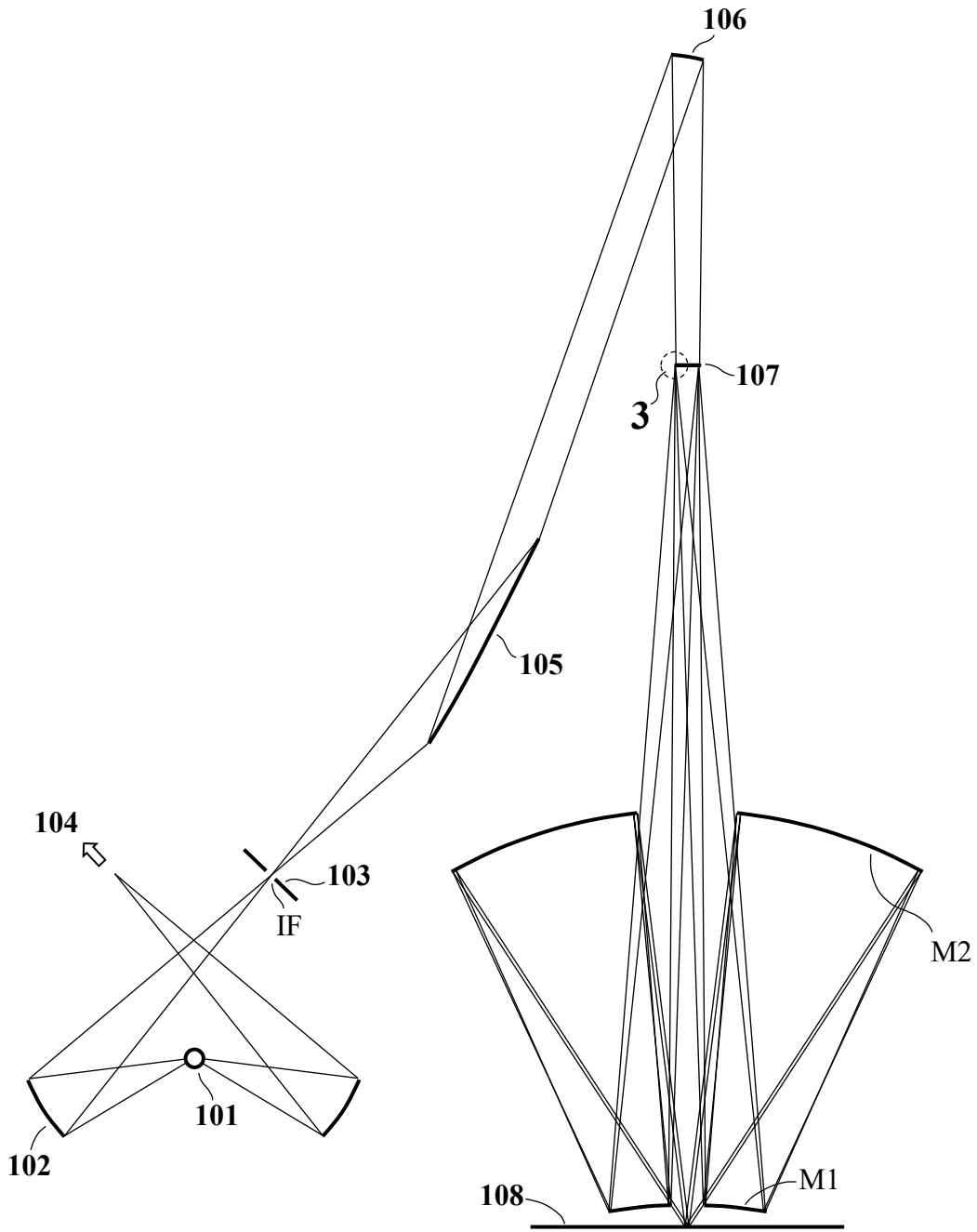


FIG. 1

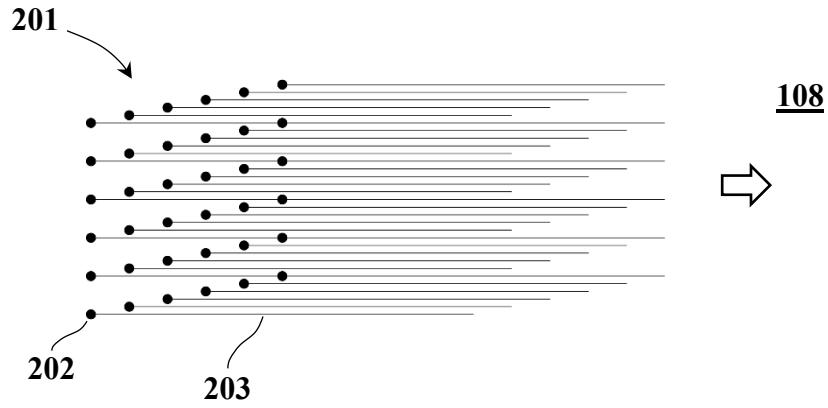


FIG. 2 (Prior Art)

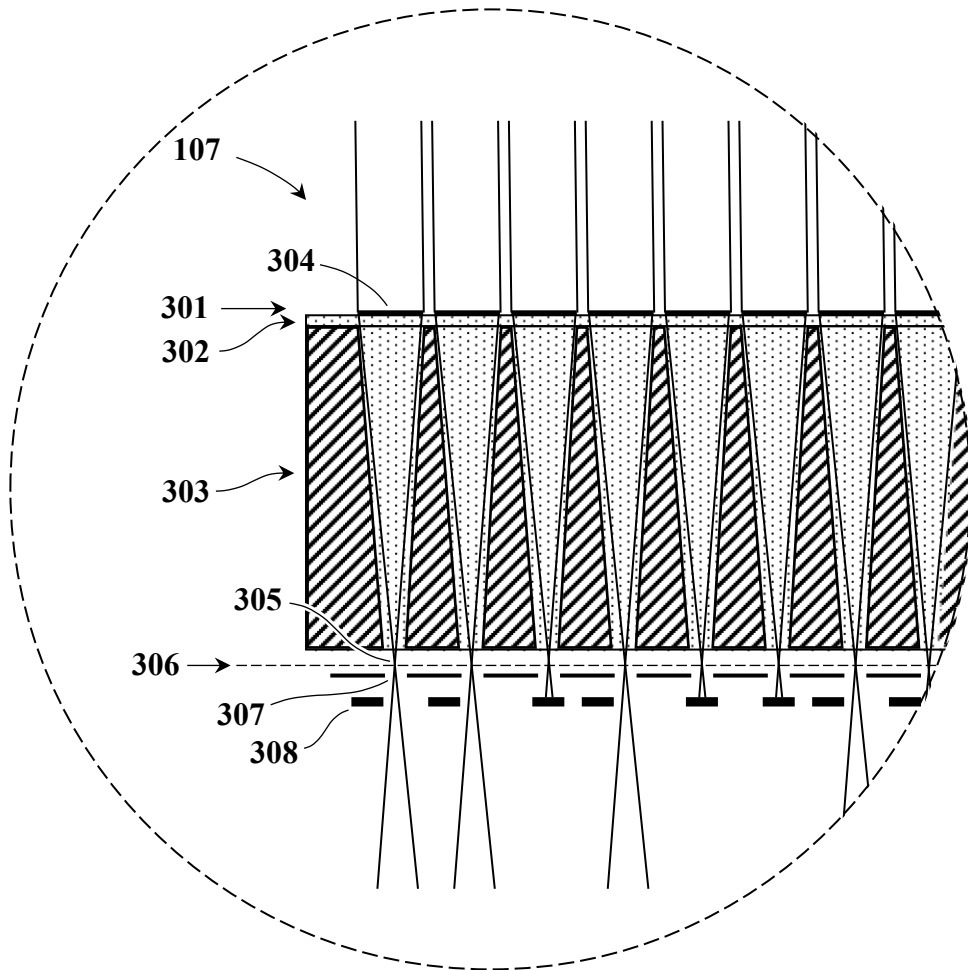


FIG. 3

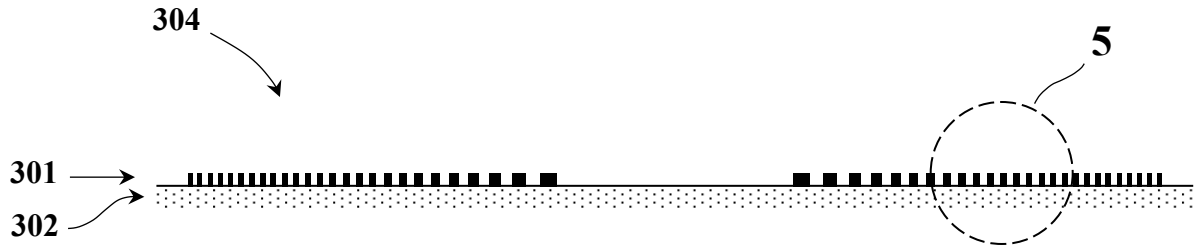


FIG. 4A

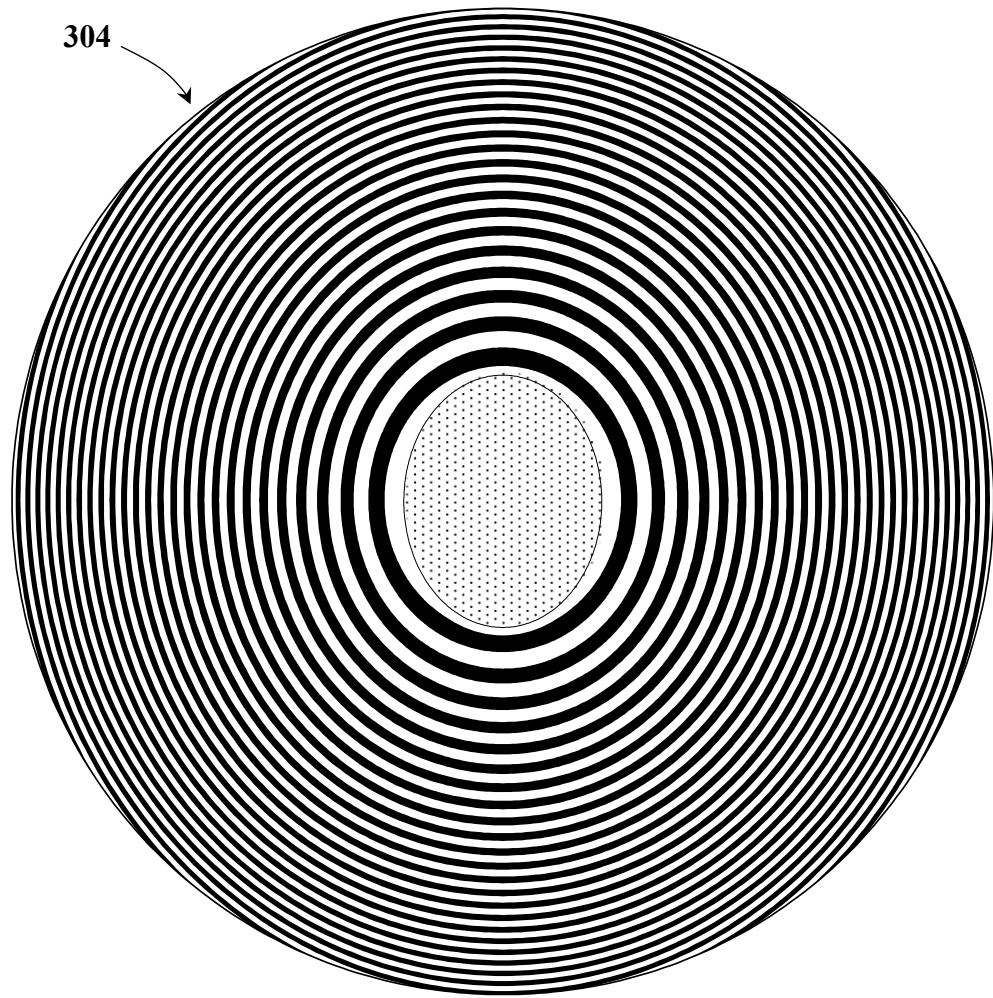


FIG. 4B

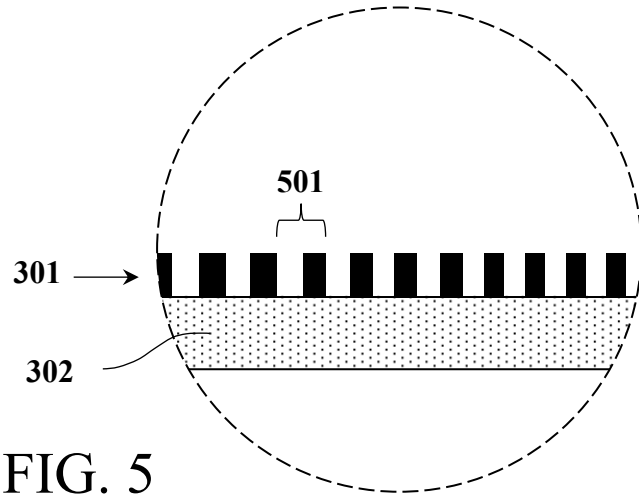


FIG. 5

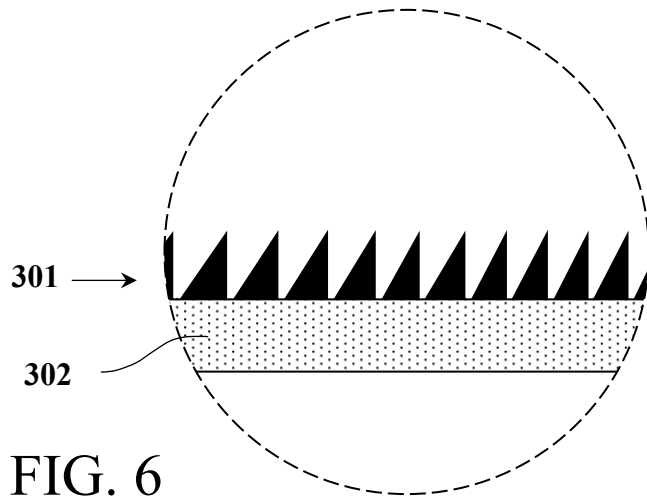


FIG. 6

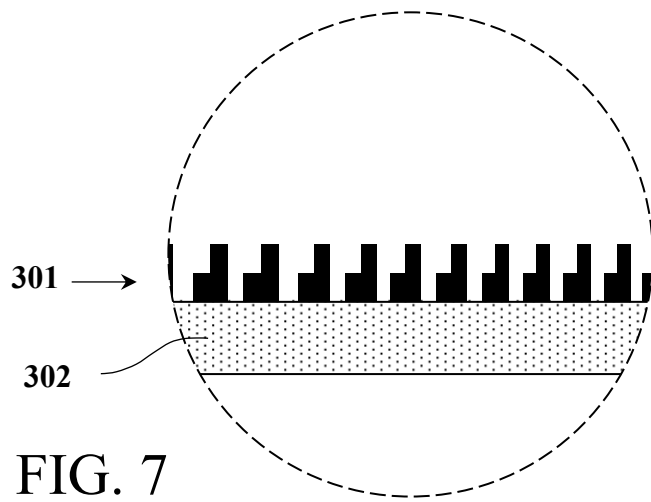


FIG. 7

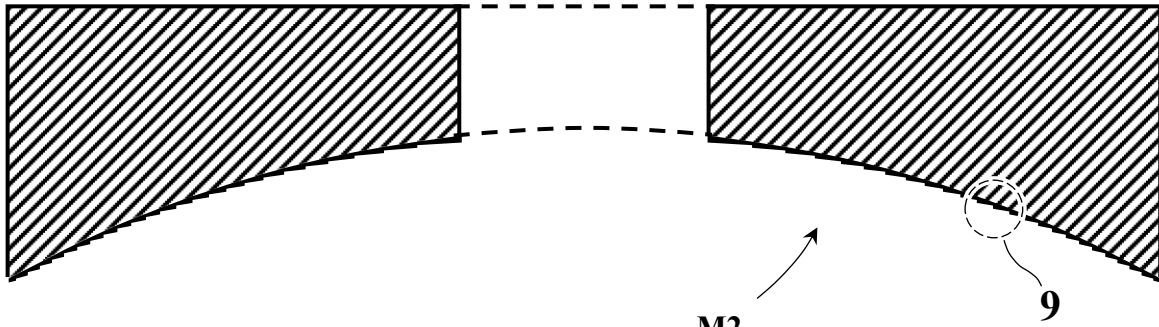


FIG. 8A

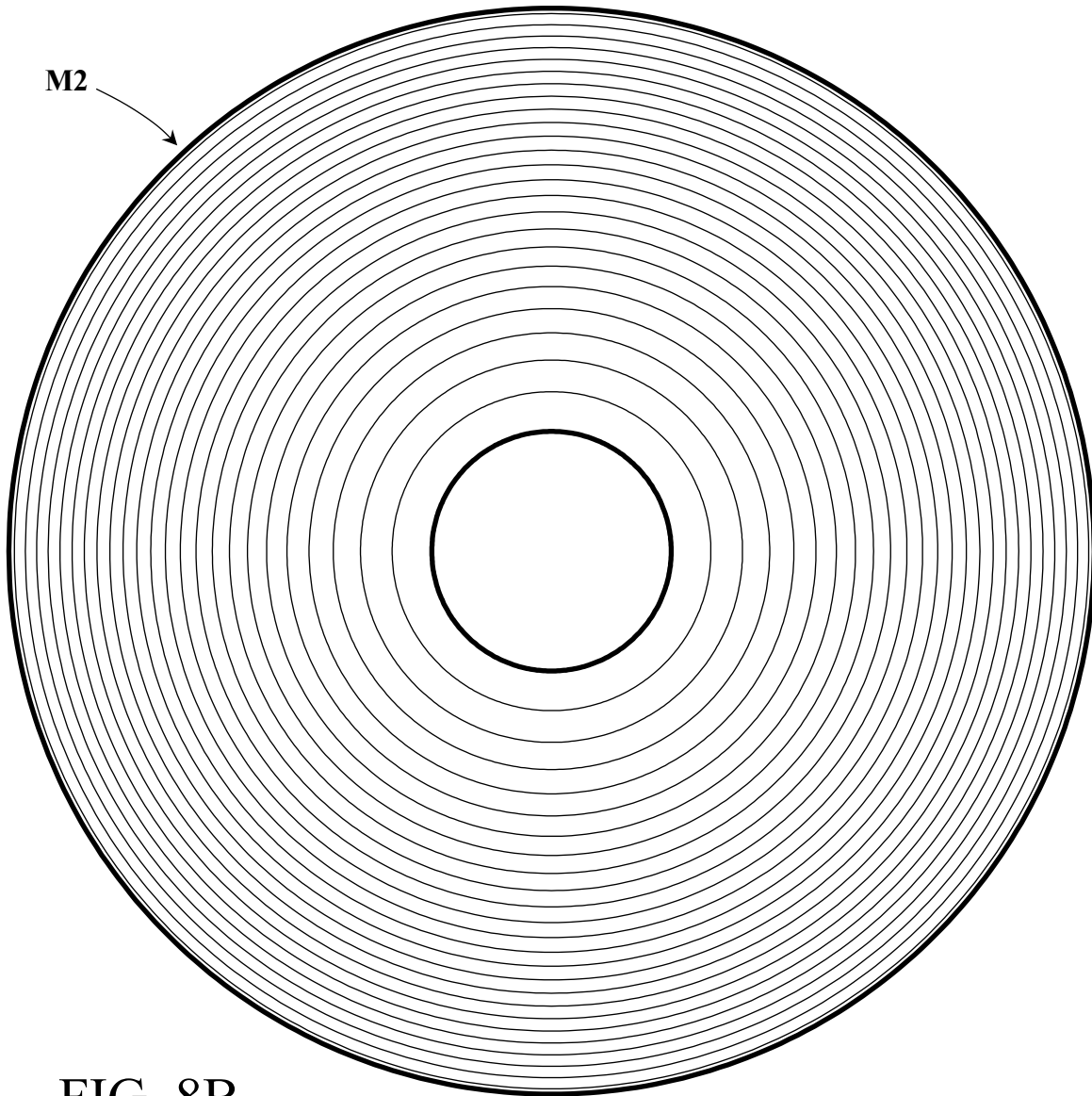


FIG. 8B

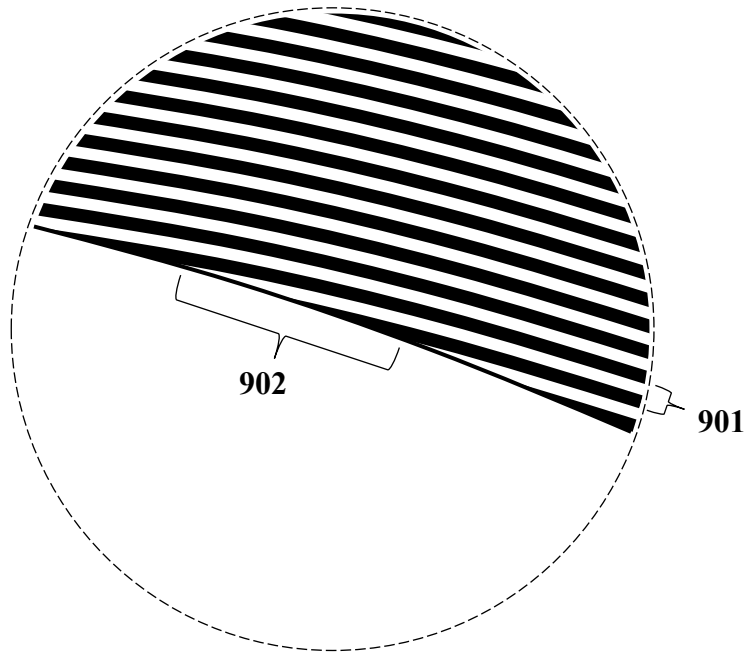


FIG. 9

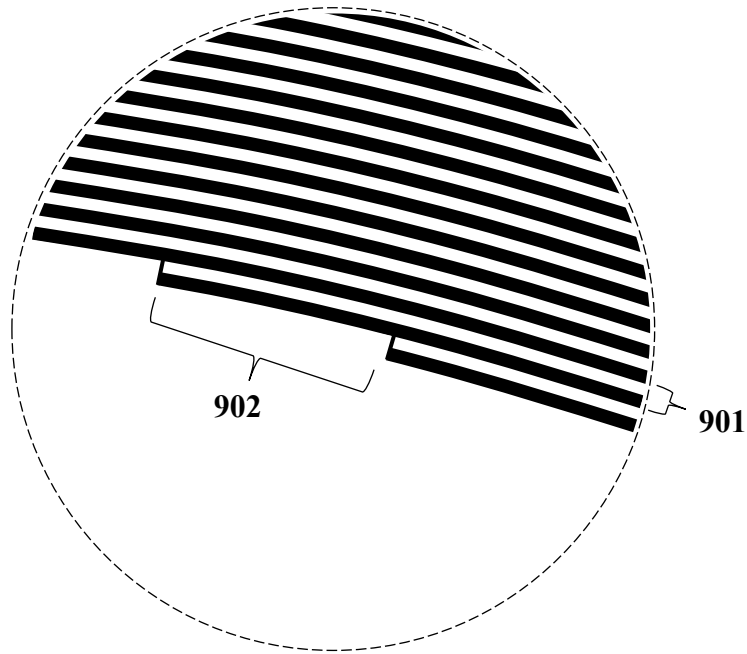


FIG. 10

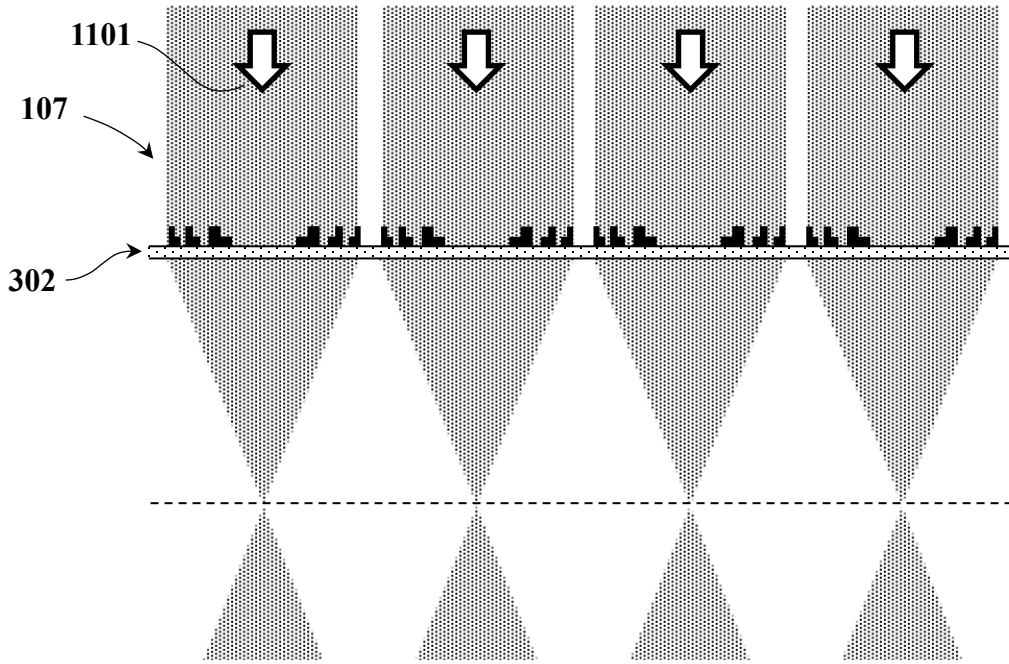


FIG. 11

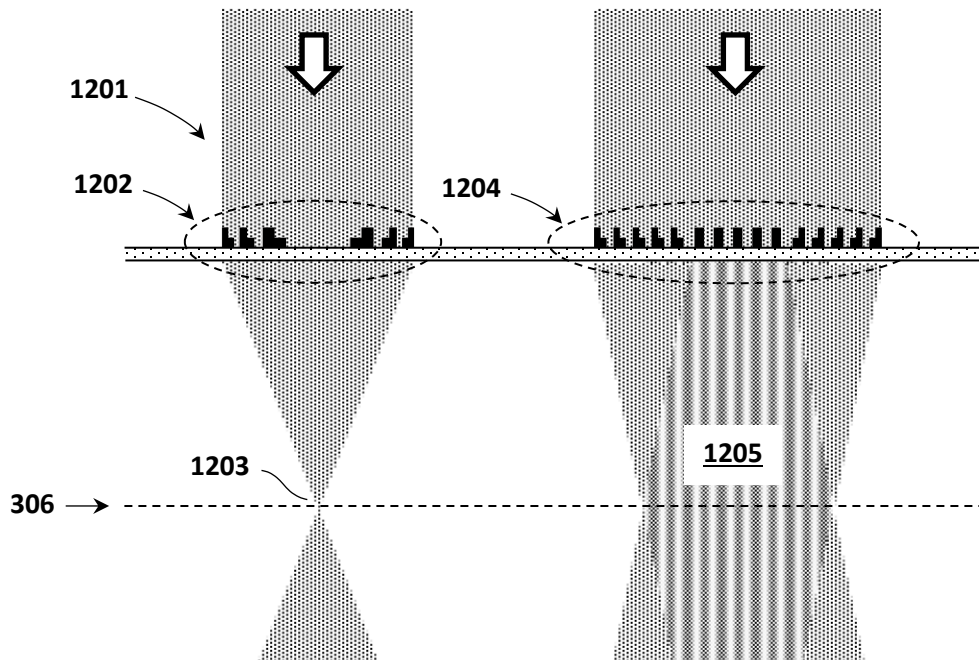


FIG. 12A

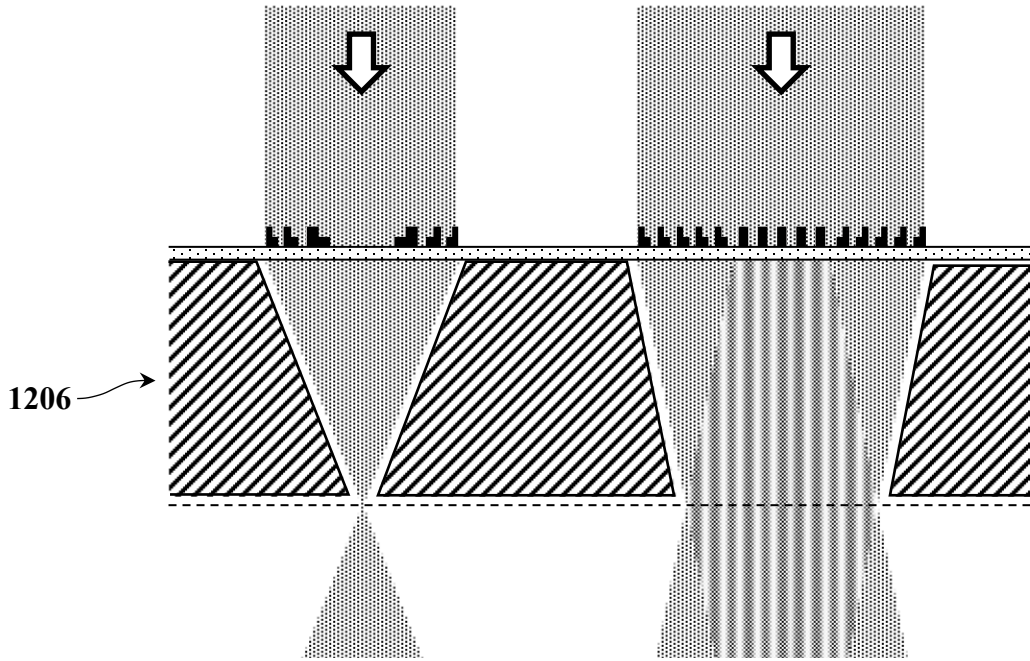


FIG. 12B

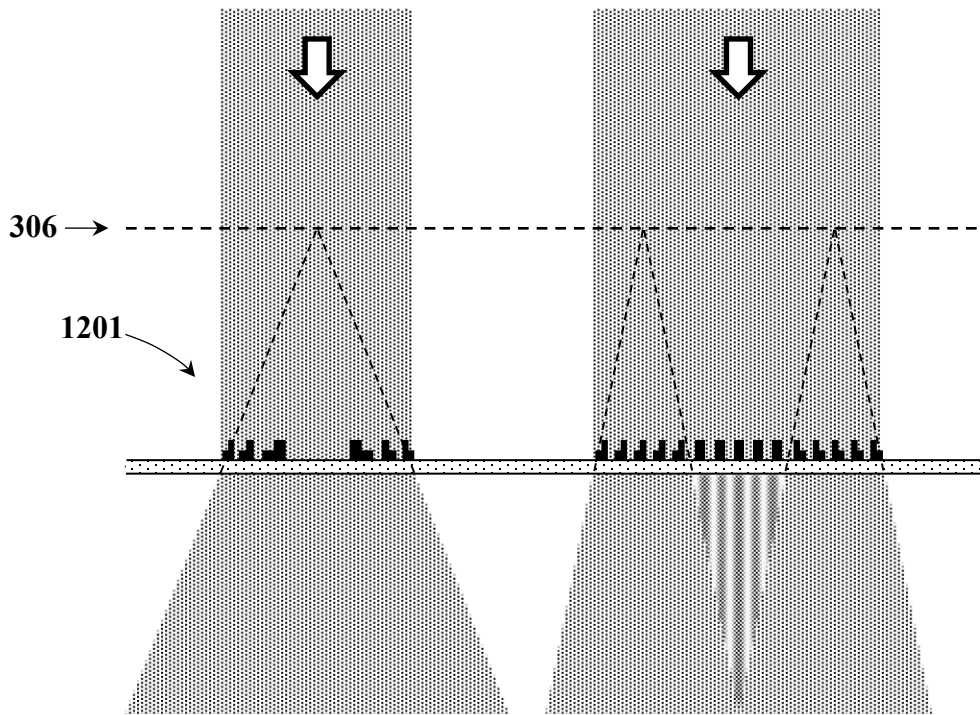


FIG. 13

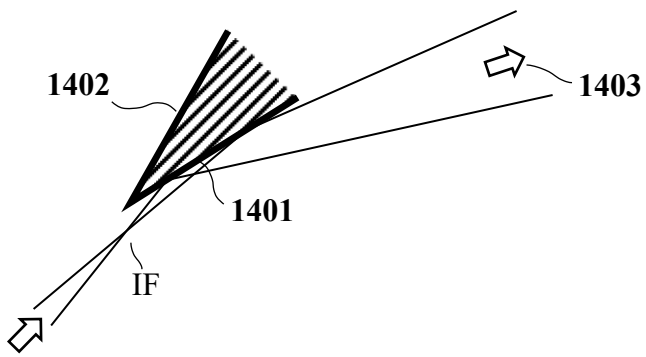


FIG. 14A

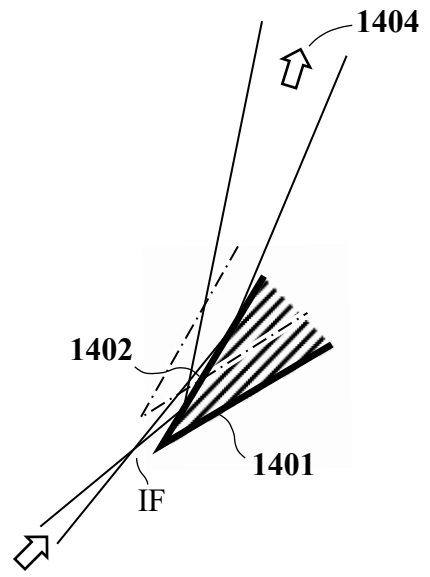


FIG. 14B

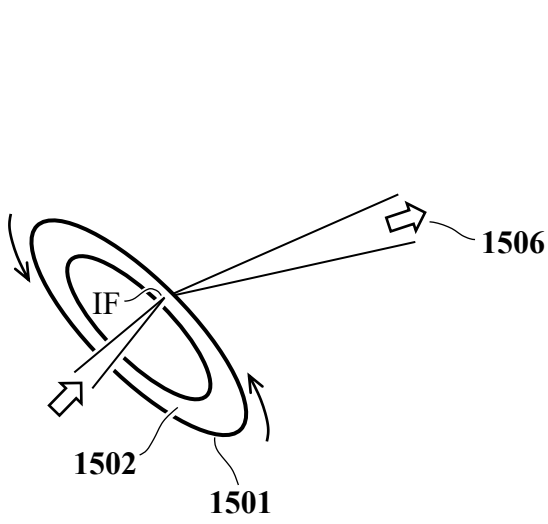


FIG. 15A

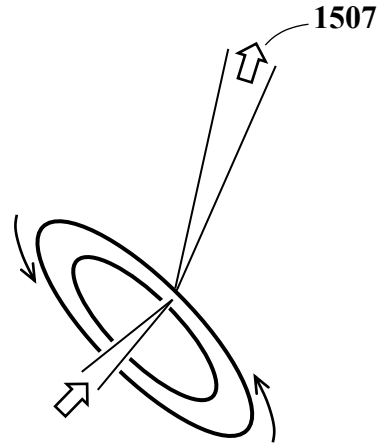


FIG. 15B

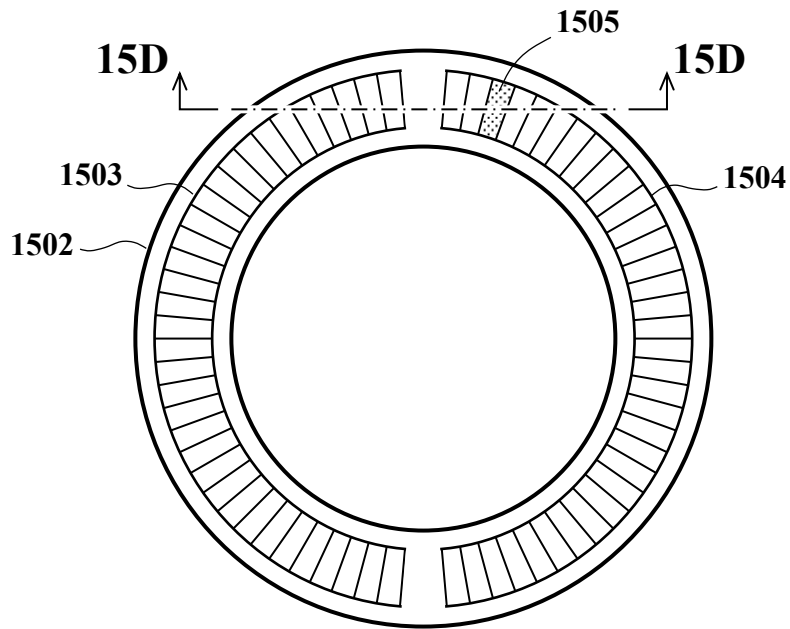


FIG. 15C

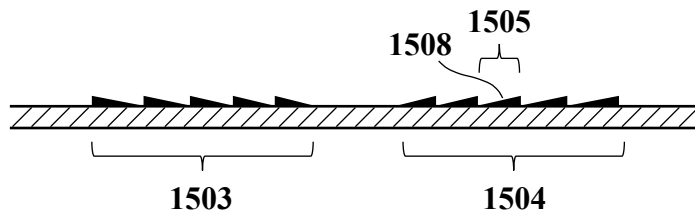


FIG. 15D

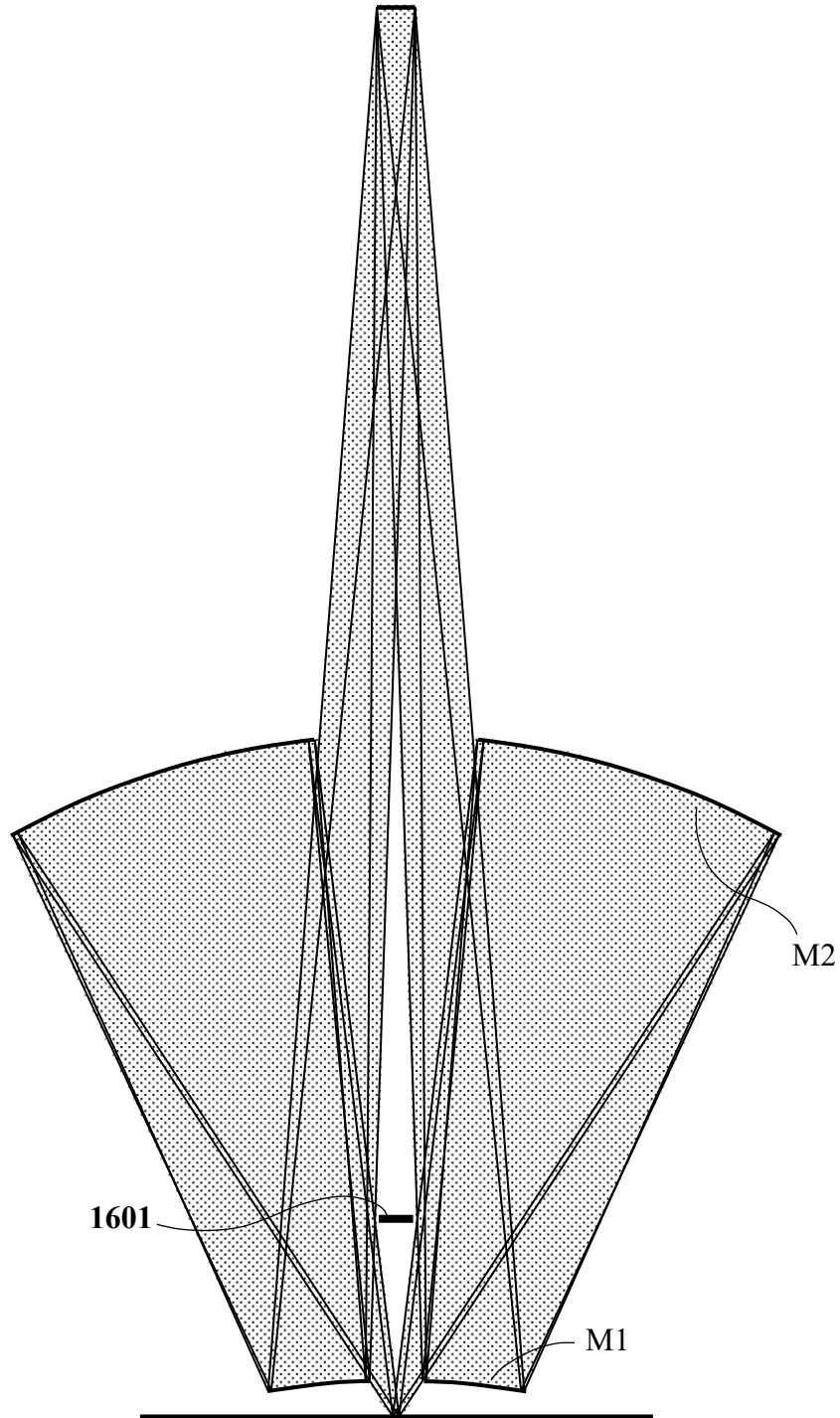


FIG. 16

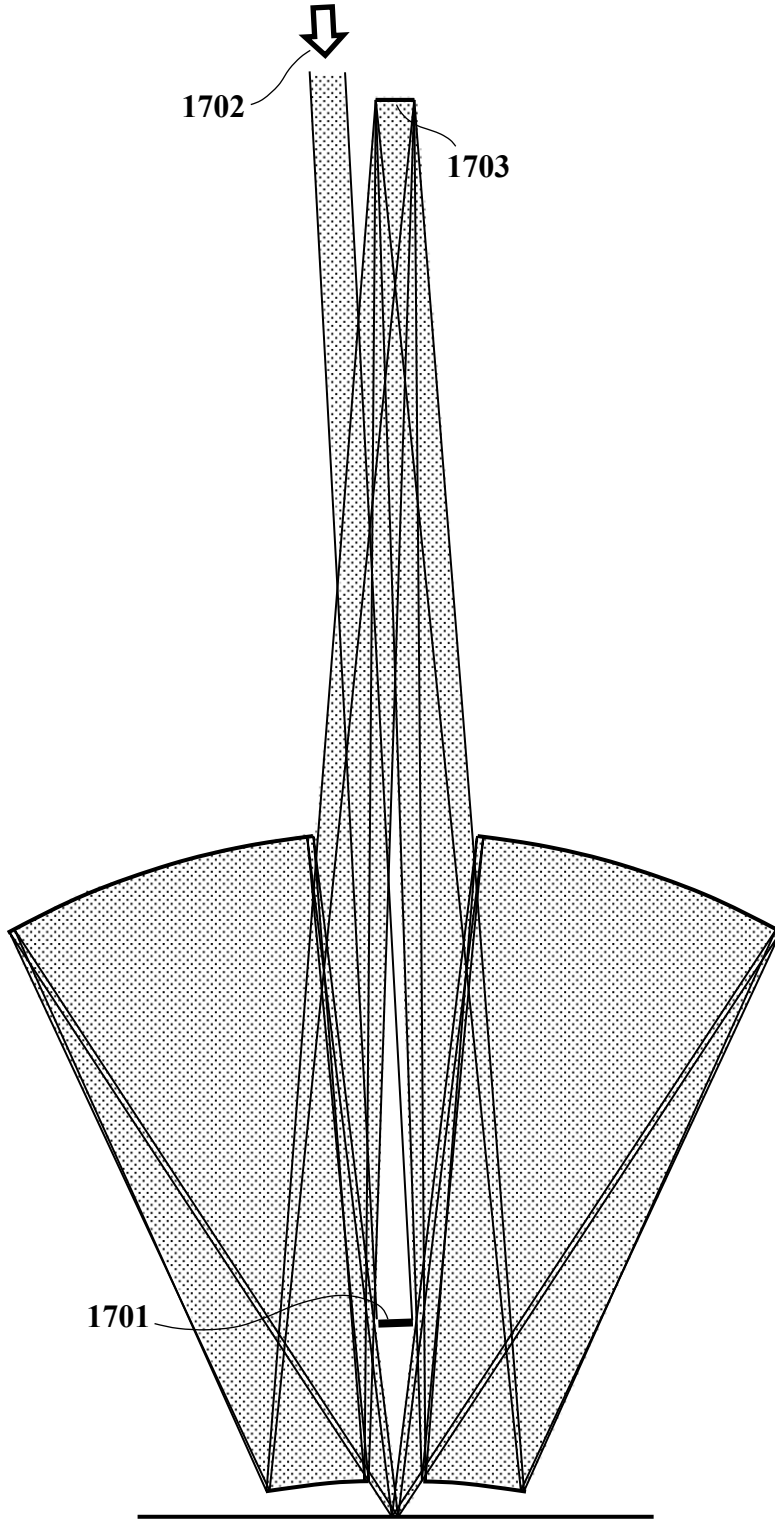


FIG. 17

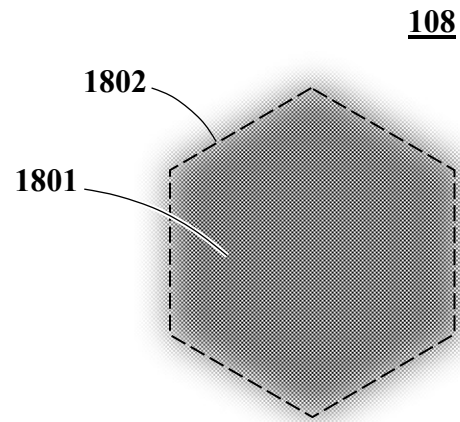


FIG. 18

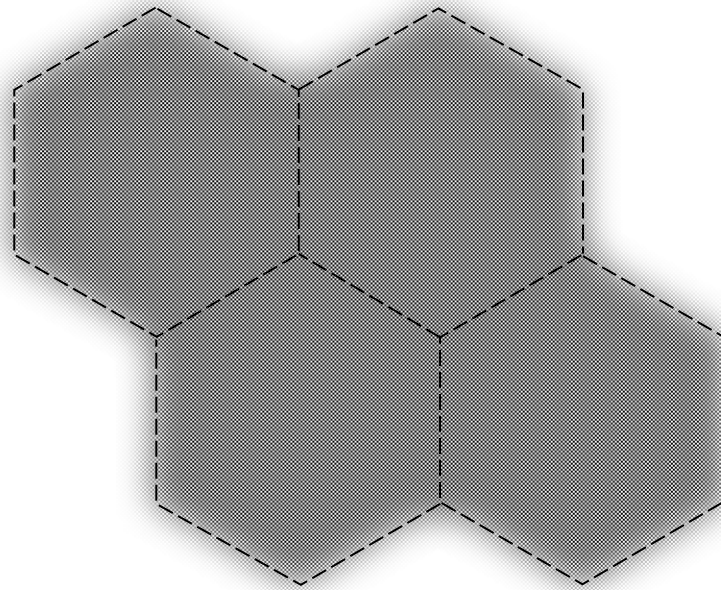


FIG. 19

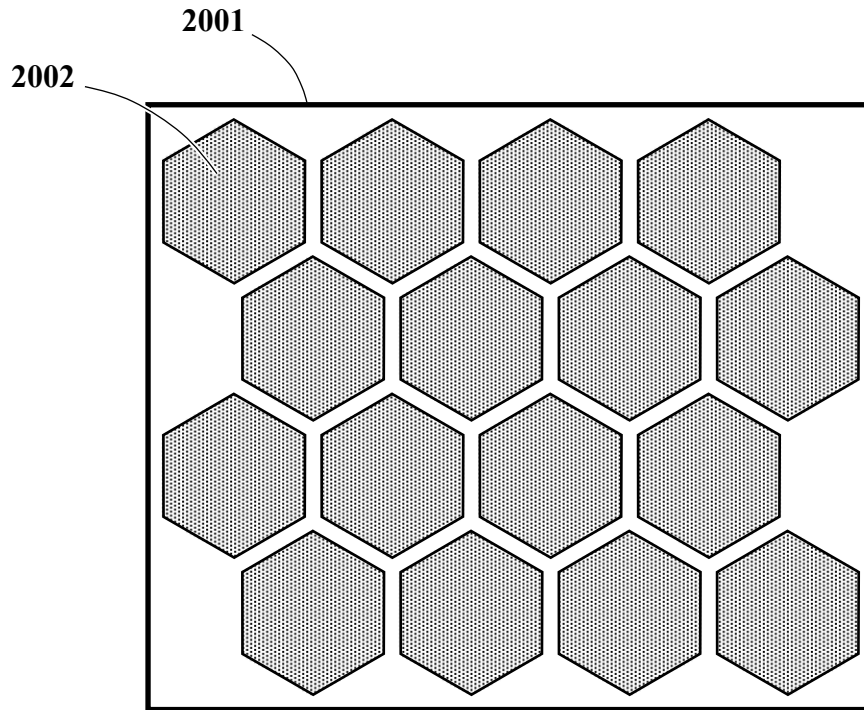


FIG. 20

$ \nabla p = 1/\lambda$	21.1
$\hat{\mathbf{u}} = \lambda \nabla p$	21.2
$ \hat{\mathbf{u}} = 1$	21.3
$N \hat{\mathbf{u}} = \hat{\mathbf{s}}(\hat{\mathbf{s}} \cdot \hat{\mathbf{u}}), T \hat{\mathbf{u}} = \hat{\mathbf{u}} - N \hat{\mathbf{u}},$ $ N \hat{\mathbf{u}} ^2 + T \hat{\mathbf{u}} ^2 = \hat{\mathbf{u}} ^2 = 1,$ $\hat{\mathbf{s}} \cdot \hat{\mathbf{u}} = \pm N \hat{\mathbf{u}} = \pm \sqrt{1 - T \hat{\mathbf{u}} ^2}$	21.4
$p'_m = p_0 + m gp$	21.5
$T \hat{\mathbf{u}}'_m = T \hat{\mathbf{u}}_0 + m \lambda T \nabla gp \quad (\hat{\mathbf{u}}_0 = \lambda \nabla p_0, \hat{\mathbf{u}}'_m = \lambda \nabla p'_m)$	21.6
$x_1 = M1_x1 + \frac{1}{2}(c_1 ss + c_2 ss^2 + \dots);$ with $ss = (x_1 - M1_x1)^2 + x_2^2 + x_3^2$	21.7
$gp = pc_1 ss + pc_2 ss^2 + \dots$	21.8

FIG. 21

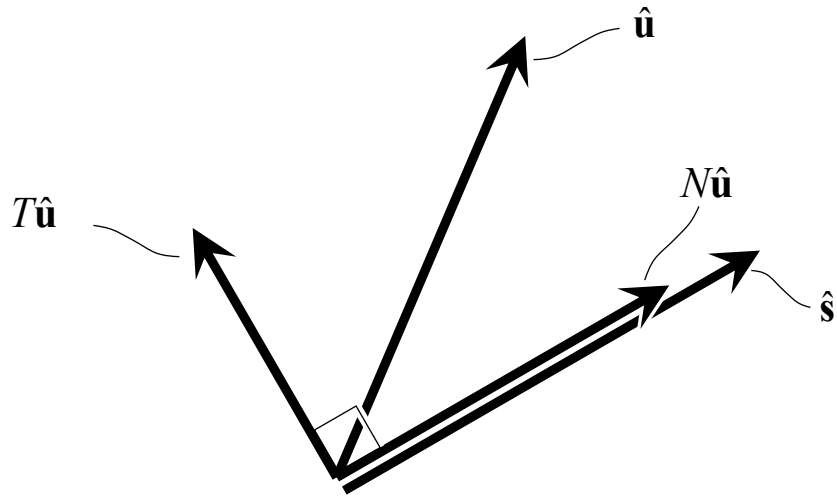


FIG. 22

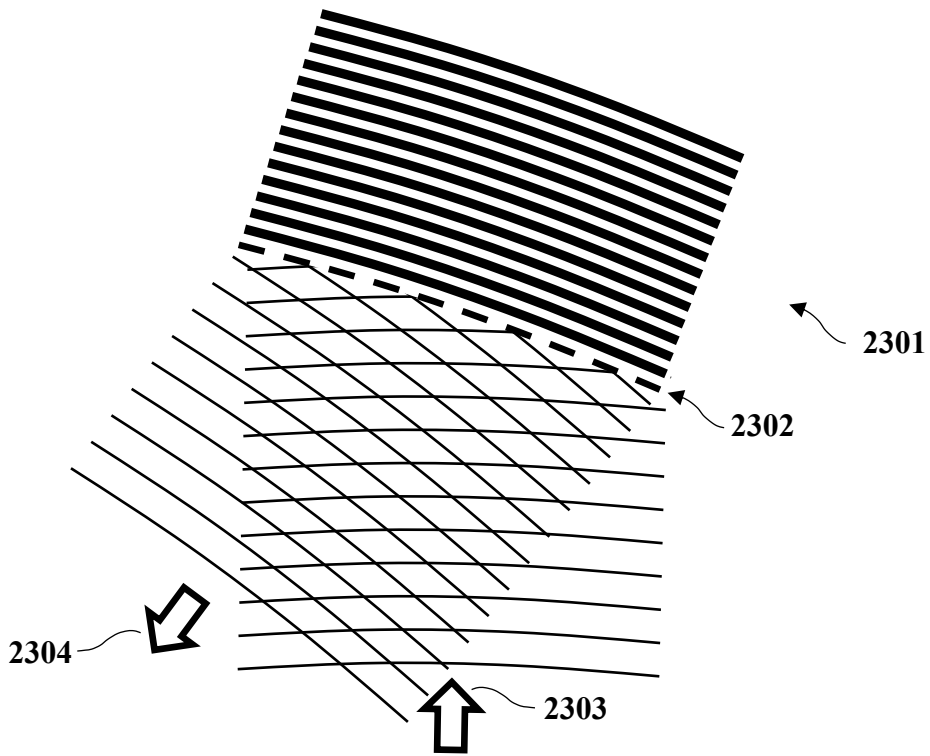


FIG. 23

Src_x1	93.069859895 mm
Lens_x1	-1096.089256032 mm
Object_x1	-1096.007867639 mm
M1_x1	-28 mm
M2_x1	-529.427845421 mm
M1 :	
c_1	0.00150026516912203 mm ⁻¹
c_2	9.14778312909296e-09 mm ⁻³
c_3	7.48343361575382e-14 mm ⁻⁵
c_4	1.0146864304588e-18 mm ⁻⁷
c_5	4.11817058645325e-24 mm ⁻⁹
c_6	6.34051703276089e-28 mm ⁻¹¹
M2 :	
c_1	0.00160628798459859 mm ⁻¹
c_2	1.13303774706633e-10 mm ⁻³
c_3	6.07101246796666e-17 mm ⁻⁵
c_4	2.35559036791934e-23 mm ⁻⁷
c_5	2.2401009173088e-29 mm ⁻⁹
pc_1	0.000997094898207104 mm ⁻²
pc_2	-1.17220997696821e- 10 mm ⁻⁴
NA	0.55
NA_inner	0.125
demag	6

FIG. 24

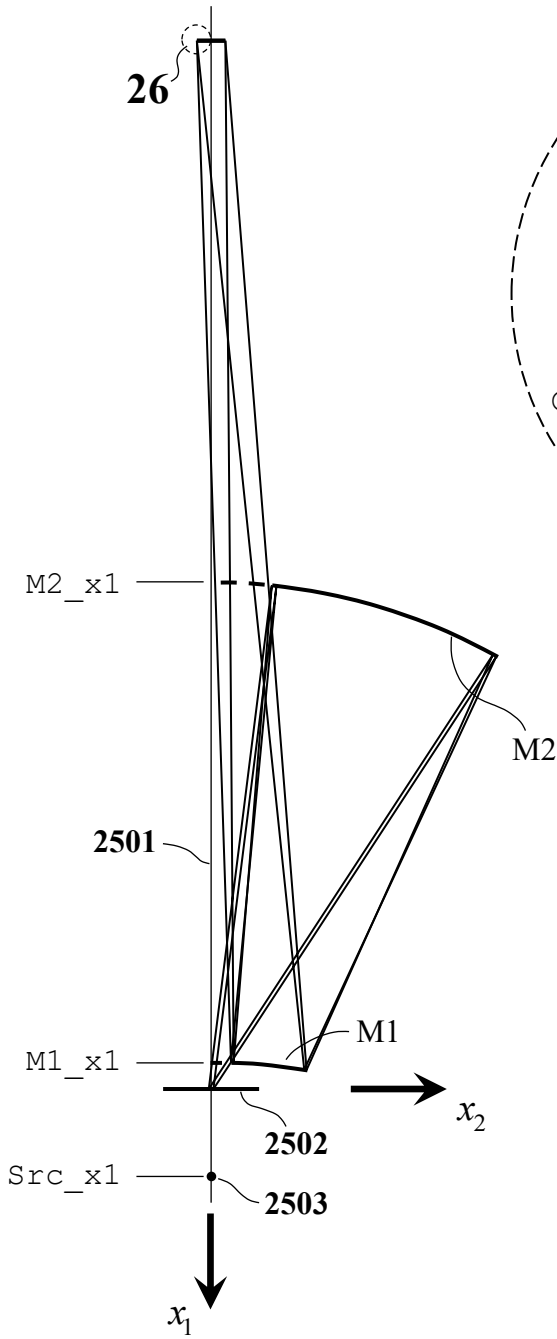


FIG. 25

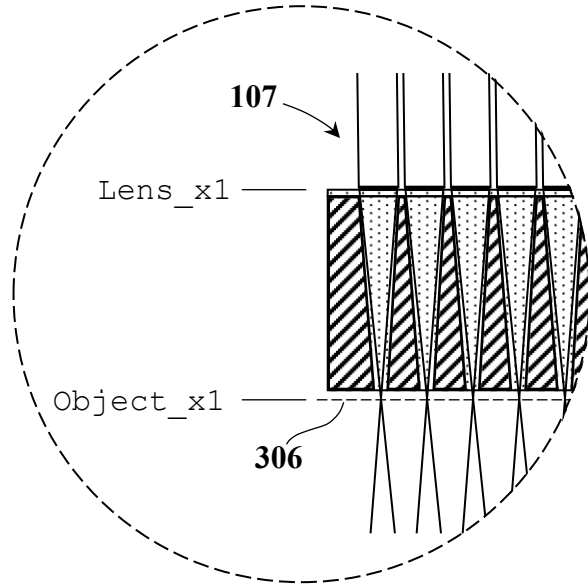


FIG. 26

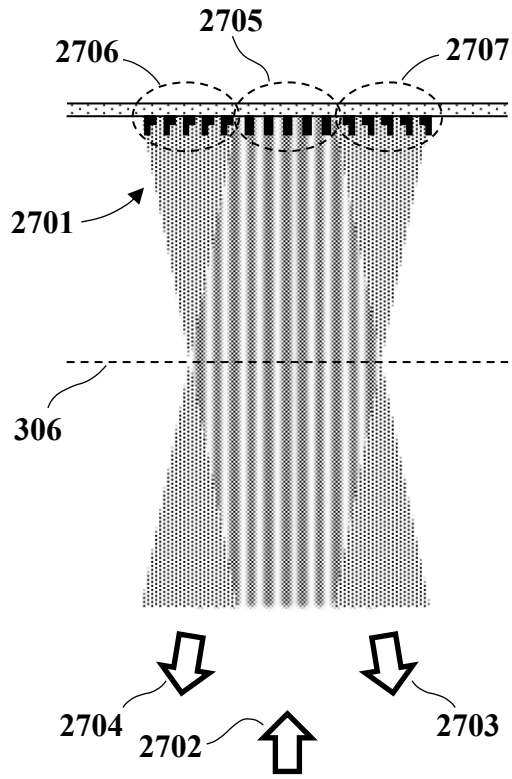


FIG. 27

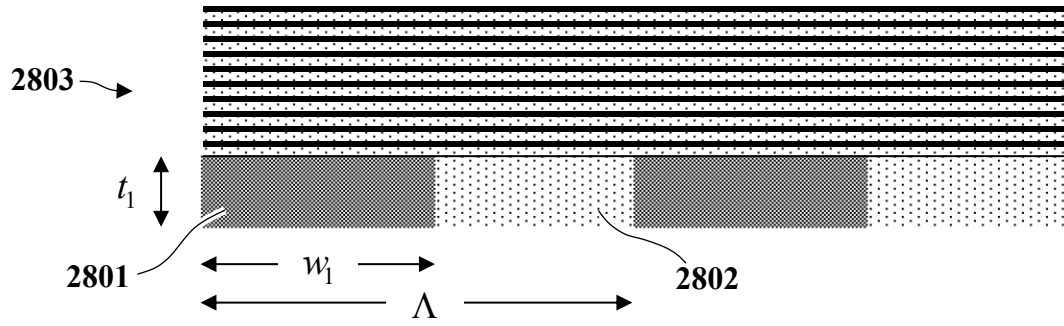


FIG. 28

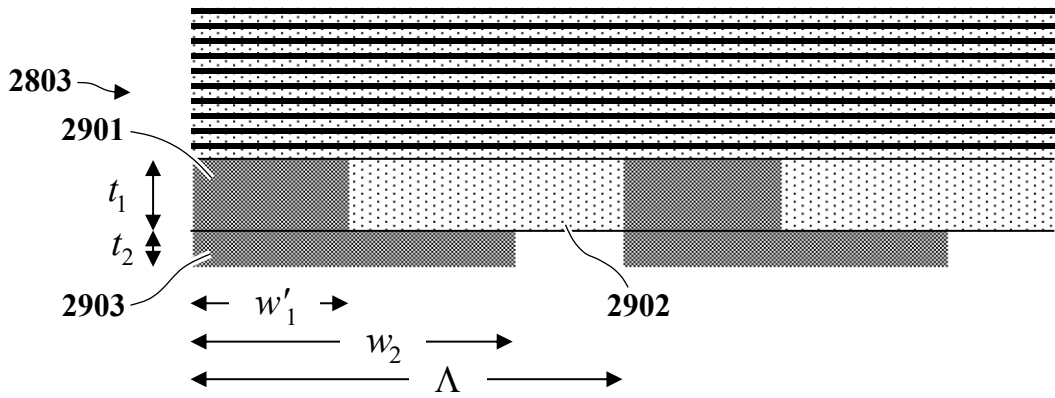


FIG. 29